Journal of Materials Chemistry B

ROYAL SOCIETY OF CHEMISTRY

PAPER

View Article Online
View Journal | View Issue

Cite this: *J. Mater. Chem. B*, 2021, **9**, 1297

Novel multi-stimuli responsive functionalized PEG-based co-delivery nanovehicles toward sustainable treatments of multidrug resistant tumor†

Jingwen Xu, *[a] Xiangji Yan,[b] Xin Ge,[c] Mingzhen Zhang,[b] Xugang Dang,[d] Yan Yang,[a] Feng Xu, *[e] Yanling Luo[e] and Guoliang Li[a]

Received 10th September 2020,
Accepted 22nd December 2020

DOI: 10.1039/d0tb02192j

rsc.li/materials-b

The efficacy of ongoing anticancer treatment is often compromised by some barriers, such as low drug content, nonspecific release of drug delivery system, and multidrug resistance (MDR) effect of tumors. Herein, in the research a novel functionalized PEG-based polymer cystine–(polyethylene glycol)$_2$-*b*-(poly(2-methacryloyloxyethyl ferrocenecarboxylate)$_2$) (Cys–(PEG$_{45}$)$_2$-*b*-(PMAOEFC)$_2$) with multi-stimuli sensitive mechanism was constructed, in which doxorubicin (DOX) was chemical bonded through Schiff base structure to provide acid labile DOX prodrug (DOX)$_2$–Cys–(PEG$_{45}$)$_2$-*b*-(PMAOEFC)$_2$. Afterwards, paclitaxel (PTX) and its diselenide bond linked PTX dimer were encapsulated into the prodrug through physical loading, to achieve pH and triple redox responsive (DOX)$_2$–Cys–(PEG$_{45}$)$_2$-*b*-(PMAOEFC)$_2^{@PTX}$ and (DOX)$_2$–Cys–(PEG$_{45}$)$_2$-*b*-(PMAOEFC)$_2^{@PTX\ dimer}$ with ultrahigh drugs content. The obtained nanovehicles could self-assemble into globular micelles with good stability based on fluorescence spectra and TEM observation. Moreover, there was a remarkable "reassembly–disassembly" behavior caused by phase transition of micelles under the mimic cancerous physiological environment. DOX and PTX could be on-demand released in acid and redox stress mode, respectively. Meanwhile, *in vivo* anticancer studies revealed the significant tumor inhibition of nanoformulas. This work offered facile strategies to fabricate drug nanaovehicles with tunable drug content and types, it has a profound significance in overcoming MDR effect, which provided more options for sustainable cancer treatment according to the desired drug dosage and the stage of tumor growth.

1. Introduction

Currently, chemotherapy, an effective therapeutic means for cancer, has been confined by water-insolubility, non-selectivity, limited stability and poor targeting of chemotherapeutic agents.[1] In the past decade, the amphiphilic polymers have been deeply investigated as a hopeful anticancer drug carriers due to its bearing both hydrophilic and hydrophobic segments,[2] providing a loading platform for hydrophobic drugs *via* chemical bonding or physical loading.[3–5] Even so, it still inevitably suffers from some drawbacks, including low drug content and the resulting insufficient drug concentration at cancerous site. To tackle these issues, although increasing drug dosage or multiple injections is an effective method for elevating local drug concentration, it could cause severe side effects and multidrug resistance (MDR) effect due to long-term usage, and ultimately compromise the treatment efficacy.[6,7]

Stimuli responsive drug delivery systems (DDSs) always contain certain components and active bonds that respond to specific physiological signals at tumor region, which is particularly appealing for cancer treatment.[8] Up to now, polymethacrylic acid and poly(2-(dimethylamino)ethyl methacrylate) have been introduced in the backbone of pH responsive polymeric DDSs to control drug release at cancerous weak acidic site by "protonation–deprotonation" circulation.[9–11] Disulfide or diselenide bond containing DDSs can be reduced into mercaptan or selenol by 2–10 mM glutathione (GSH), and the latter also can be oxidized into selenic acid by 10–100 μM H_2O_2 ROS. Specially, the bonding energy of

[a] *School of Food and Biological Engineering, Shaanxi University of Science and Technology, Xi'an 710021, China. E-mail: xujingwen@sust.edu.cn*
[b] *Institute of Medical Engineering, School of Basic Medical Sciences, Xi'an Jiaotong University, Xi'an, Shaanxi Province, China*
[c] *The First Affiliated Hospital of USTC, Division of Life Science and Medicine, University of Science and Technology of China, Hefei, Anhui, 230001, China*
[d] *College of Bioresources Chemical and Materials Engineering, Shaanxi University of Science & Technology, Xi'an 710021, China*
[e] *Key Laboratory of Macromolecular Science of Shaanxi Province, School of Chemistry and Chemical Engineering, Shaanxi Normal University, Xi'an 710062, China. E-mail: fengxu@snnu.edu.cn*

† Electronic supplementary information (ESI) available. See DOI: 10.1039/d0tb02192j

diselenide bond is lower than that of disulfide bond, leading to a smart redox responsive behavior and synchronous drug release when diselenide bonds contained carrier crack. After that, selenium in carriers not only can be used to enrich the trace elements that necessary to body, but also relieve multidrug-resistance (MDR) effect.[6,12,13] As a kind of famous eletroactive component, ferrocene is liable to oxidize into ferrocenium by H_2O_2, $KMnO_4$, NaClO and $FeCl_3$, and it is apt to be reduced into ferrocene by vitamin C inversely.[14,15] Based on few previous studies, the synergistic of ferrocene contained DDSs responded to dual and even multiple special physiological signals will be an effective strategy for realizing site-specific, controlled and targeted release.[16]

Polymeric DDSs constructed *via* physical loading are always of low drug content than 20% and poor stability due to drug bound with polymer through π–π stacking, hydrophobic and hydrogen bonding interactions, even though the prodrug can be a promising vehicle by chemical bonding between drug and polymer.[17,18] Meanwhile, the inadequate reactive sites of prodrugs in polymer backbone also restrict the increase of drug content.[19–22] Sun *et al.* fabricated a disulfide bond linked camptothecin (CPT) prodrug PCPTSP-*co*-PEEP with CPT content ranged from 7.8–27.2%.[23] Generally, a feasible approach to prodrug functionalization is to introduce various of stimulus responsive linkages such as hydrazone, disulfide, diselenide bond and so on,[24–26] the resulting prodrugs can be broken under their corresponding physiological stimulus. However, it is still a pendent problem that an uncertain induction process retards the whole release behavior. DDSs with PEG shell are particularly hidden and can prevent aggregation,[27,28] prolong circulation time, and avoid clearance through making DDSs highly resistant to protein adsorption.[29,30] In addition, drug loading and release behavior are optimized by providing a physico-chemical barrier to drug leak *via* PEG,[31–33] and the electrostatic and steric hindrances of PEG improve transport coefficients in mucus, obtaining a satisfactory drug delivery efficacy.[34–36]

Based on the complications of cancer therapy and MDR effect, in the research such novel polymeric carriers are expected to have three main advantages: (1) good stability due to a reasonable hydrophobic/hydrophilic blocks balance, (2) adjustable drug types and content thanks to drug and its dimer encapsulation through chemical bonding and physical loading, and (3) desired release behavior triggered by cancerous physiological signals. For this aim, the combination of triple redox responsive mechanism including ferrocene, disulfide and diselenide groups has great significance for specific, targeted and controlled drug release, which can conduce to enhance drug delivery efficacy through synergistic effect. Various of evidences showed that the enhanced activity of efflux pumps is one of the most common mechanisms involved in cancer processes. Meanwhile, the membrane transport proteins (particularly P-glycoprotein) can able to recognize and expel various of exogenous hydrophobic drug molecules (such as PTX, DOX, docetaxel and so on) out of the cell. Previous researches indicated that the selenium compounds have a significant inhibitory ability to reverse MDR.[37,38] In addition, a rich variety of drugs and high drug loading content can overcome MDR *via* rapid intracellular drug delivery.[39,40] Herein, a PEG-based doxorubicin (DOX) prodrug containing hydrazone (doxorubicin)$_2$–cystine–(polyethylene glycol)$_2$-*b*-(poly(2-methacryloyloxyethyl ferrocenecarboxylate)$_2$) ((DOX)$_2$–Cys–(PEG$_{45}$)$_2$-*b*-(PMAOEFC)$_2$) was prepared. With respect to the different therapeutic mechanism of both DOX and paclitaxel (PTX),[41–43] and the potential of dual drugs co-delivery system for overcoming MDR effect, diselenide bond linked PTX (PTX dimer) was synthesized, followed by encapsulating into the obtained prodrug through hydrophobic, π–π stacking and hydrogen bonding interactions. This system can afford a dual drugs co-delivery system (DOX)$_2$–Cys–(PEG$_{45}$)$_2$-*b*-(PMAOEFC)$_2$$^{@PTX\,dimer}$ with 39.3% of DOX and 49.1% of PTX, this value far exceeds those reported elsewhere.[23,44] It can self-assemble into globular micellar aggregates bearing DOX, hydrophobic core of DOX, PTX, PMAOEFC and hydrophilic PEG shell in aqueous solution, and critical micellar concentration as low as 5.78 mg L^{-1} from fluorescence spectrum. Due to the presence of Schiff base structure, the break of hydrazone bond and resulting pH induced DOX diffuse behavior were confirmed by ^{1}H NMR, dynamic light scattering (DLS) and fluorescence spectrums. Additionally, the micellar disassembly-reassembly process caused by triple redox responsiveness was investigated by DLS, TEM and cyclic voltammetry (CV). Results found that it is a valid strategy to develop DDS with high drug content. The prepared nanovehicles had good stability and satisfactory therapeutic effect by designing stimuli responsive polymer and loading hydrophobic drug dimer afterwards, which can also make up the deficiency of delayed drug release of prodrugs and evade MDR effect, realizing a sustained, on-demand and targeted release. The research opens up a variety of treatment modes to tumors at different stages.

2. Materials and methods

2.1 Materials and reagents

(Boc–Cys–OH)$_2$ (98%), trifluoroacetic acid (TFA, 99%), tetrabutylammonium hexafluorophosphate (TBAHFP, 98%), glutathione (GSH, 98%) and L-ascorbic acid (Vc, >99.0%) were provided by Shanghai Macklin Biochemical Co., Ltd (Shanghai, China). Polyethylene glycol 2000 (PEG2000), 2-bromoisobutyryl bromide (BiBB, 98%), paclitaxel (PTX, 98%), doxorubicin hydrochloride (DOX·HCl, 98%) were purchased from J&K Chemical Ltd (Beijing, China). Sodium borohydride ($NaBH_4$, 96%), anhydrous sodium sulfate (Na_2SO_4, ≥99.0%), dichloromethane (DCM), *N*,*N*′-dimethylformamide (DMF), tetrahydrofuran (THF) and triethylamine (TEA) were supplied by Sinopharm Chmical Reagent Co. Ltd (Shanghai, China). DCM was pre-dried in anhydrous Na_2SO_4, and then purified in CaH_2 for 4–5 h to remove moisture. For DMF, were also dried over CaH_2 and reduced pressure distilled prior to use. 3-(4,5-Dimethyl-thiazol-2-yl)-2,5-diphenyl tetrazolium bromide (MTT, 98%) was provided by Sigma and without further treatment. Unless otherwise specified, all other chemicals were brought from commercial supplier and without additional purification.

2.2 Cells and animals

The human cervical cancer cell line HeLa and murine breast cancer cell line 4T1 were offered by Mingjin Biology (Shanghai, China). The cells were cultured in RPMI 1640 supplemented with 10% fetal calf serum (Gibco, America) under the humidified conditions containing 5% CO_2 atmosphere. Digestion and selection of cells were carried out during exponential growth phase for *in vitro* MTT assay and *in vivo* antitumor experiments.

Male Balb/c mice (20 ± 2 g) were purchased from Laboratory Animal Center of Xi'an Jiaotong University and picked for establishing 4T1 tumor bearing model. Animals were fed with chow and water under the condition of 25 °C and 55% humidity. All animal experiments were performed under the permission of the Experimental Animal Ethics Committee of Xi'an Jiaotong University Health Center. The mice were devided randomly into 7 groups (n = 5), 100 μL of 4T1 cell suspension with 1×10^6 cells was inoculated subcutaneously at the armpit of mice afterwards. All treatments were performed when the tumor size was approximately 100 mm^3 (tumor size = $ab^2/2$, wherein a and b denote the longest and shortest edge of tumor, respectively).

2.3 Synthetic procedure

The Schiff based linked DOX prodrug $(DOX)_2$-*b*-Cys-$(PEG)_2$-*b*-$(PMAOEFC)_2$ was synthesized in line with the route shown in Scheme 1.

2.3.1 Synthesis of $(Boc)_2$–Cys–$(PEG_{45})_2$. $(Boc–Cys–OH)_2$ (0.30 g, 0.68 mmol) and PEG (3.26 g, 1.63 mmol) were dissolved in anhydrous DCM (50 mL), then *N*,*N*′-dicyclohexycarbodiimide (DCC, 0.42 g, 2.05 mmol) was added into the above solution with nitrogen inletting. After stirring for 48 h at 25 °C, insoluable *N*,*N*′-dicyclohexylurea (DCU) was removed by filtration, the mixture was precipitated in excess ether thrice, collected and vacuum-dried overnight at 25 °C to afford white solid. Afterwards, the crude product was purified by encasing in dialysis tube (MWCO = 3500 Da) and dialyzed against 2000 mL of deionized water for 72 h to remove the unreacted PEG, followed by collecting the dialysate, freeze drying, to afford $(Boc)_2$–Cys–$(PEG_{45})_2$. (Yield: 31%) (^{1}H NMR: 300 MHz, $CDCl_3$), δ (ppm): 3.55–3.77 (s, 180H, –C$\underline{H}_2$C$\underline{H}_2$OH in PEG2000), 3.18 (m, 2H, –S$\underline{CH}_2$CH(NHBoc)– in (Boc–Cys–OH)$_2$), 1.45 ppm (s, 9H, C($\underline{CH}_3$)$_3$OOC–); FTIR (film): ν (cm^{-1}): 1007–1214 (C–O stretching vibration), 1726 (ester –C═O), 2848–2981 (–C–H stretching vibration), 3080–3755 (–OH).

2.3.2 Synthesis of macromolecular initiator $(Boc)_2$–Cys–$(PEG_{45})_2$–Br_2. $(Boc)_2$–Cys–$(PEG_{45})_2$ (1.00 g, 0.227 mmol) was dissolved in anhydrous DCM (8 mL) with stirring. Dissolved BiBB (84.17 μL, 0.681 mmol) in DCM (3 mL) was dropwise added in the above solution with nitrogen inletting at 0 °C. Following TEA (126 μL, 0.908 mmol) in DCM (2 mL) was dropwise added into the mixed liquor. The reaction was carried out at 25 °C for 24 h. The resulting mixture was filtrated, removed solvent by rotary evaporation, and precipitated using excess ether for several times, dried at 25 °C for 24 h to afford white solid $(Boc)_2$–Cys–$(PEG_{45})_2$–Br_2. (Yield: 36%) (^{1}H NMR: 300 MHz, $CDCl_3$), δ (ppm): 1.87 (s, 6H, –C($\underline{CH}_3$)$_2$Br from BiBB residues).

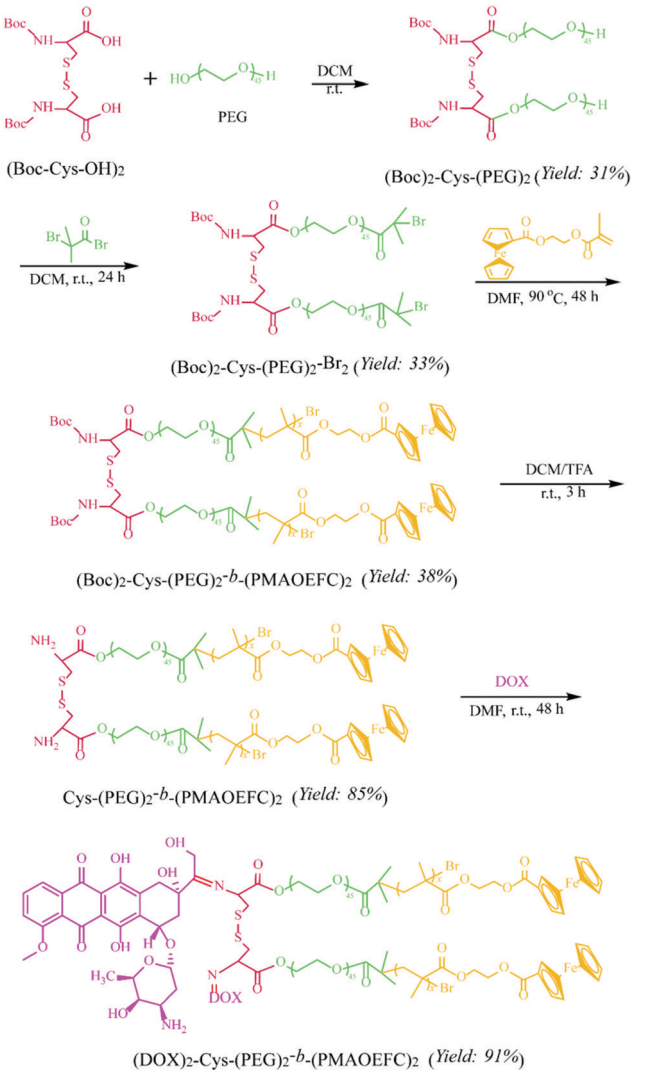

Scheme 1 Synthetic route of Schiff base linked DOX prodrug $(DOX)_2$–Cys–$(PEG)_2$-*b*-$(PMAOEFC)_2$.

2.3.3 Synthesis of $(Boc)_2$–Cys–$(PEG_{45})_2$-*b*-$(PMAOEFC)_2$. The synthesis procedure of ferrocene monomer 2-methacryloyloxyethyl ferrocenecarboxylate (MAOEFC) was depicted in ESI.† The amphiphilic block copolymer $(Boc)_2$–Cys–$(PEG_{45})_2$-*b*-$(PMAOEFC)_2$ was synthesized through atom transfer radical polymerization (ATRP). Specifically, macromolecular initiator $(Boc)_2$–Cys–$(PEG_{45})_2$–Br_2 (0.30 g, 6.38×10^{-2} mmol) and monomer MAOEFC (1.75 g, 5.10 mmol) were dissolved in anhydrous DMF (6 mL), and then transferred into a 25 mL of Schlenk flask. Subsequently, PMDETA (79.5 μL, 0.383 mmol) and CuCl (31.6 mg, 0.319 mmol) were added swiftly under nitrogen atmosphere. After that, "freeze–pump–thaw" cycles were performed thrice to expel oxygen in the system. After the reaction proceeded at 90 °C for 48 h, the mixture was diluted with THF, and then passed through neutral aluminum column to remove ligand and catalyst. The mixture was rotary evaporated and repeatedly purified by precipitating in excess ice ether thrice, the final brown precipitate was vacuum dried at 40 °C for 24 h. (Yield: 38%) (^{1}H NMR: 300 MHz, $CDCl_3$), δ (ppm): 1.68 (56H, m, –$\underline{CH}_2$C(CH_3) BrCOO– in main chains),

1.09 (84H, m, –$CH_2C(\underline{CH_3})$BrCOO–), 4.40 (112H, m, –COO$\underline{CH_2}\underline{CH_2}$-OCO–), 4.04 (5H in ferrocenyl protons), 4.20 (2H, s, *meta*-H in Cp rings), 4.80 (2H, s, *ortho*-H in Cp rings); FTIR (film): ν (cm^{-1}): 427–548 (Fe-Cp), 2864–2949 (–C–H stretching vibration), 1717 (ester –C═O), 3099 (═C–H), 1638 (C═C), 1061–1211 (C–O stretching vibration), 783–862 (bending vibration of ═C–H in Cp rings).

2.3.4 Synthesis of Cys–$(PEG_{45})_2$-*b*-$(PMAOEFC)_2$. Cys–$(PEG_{45})_2$-*b*-$(PMAOEFC)_2$ was achieved through the deprotection of $(Boc)_2$–Cys–$(PEG_{45})_2$-*b*-$(PMAOEFC)_2$. Typically, $(Boc)_2$–Cys–$(PEG_{45})_2$-*b*-$(PMAOEFC)_2$ (0.98 g, 0.041 mmol) was dissolved in DCM–TFA mixed solvent (15 mL, ν_{DCM}/ν_{TFA} = 2/1), the reaction was performed at 25 °C. After 3 hours, the mixture was concentrated *via* rotary evaporation, then precipitated in excess ether thrice, and vacuum dried to afford black solid Cys–$(PEG_{45})_2$-*b*-$(PMAOEFC)_2$, which was represented as P hereinafter. (Yield: 85%) (^{1}H NMR: 300 MHz, $CDCl_3$), δ (ppm): 4.20 (5H in ferrocenyl protons), 4.34 (2H, s, *meta*-H in Cp rings), 4.80 (2H, s, *ortho*-H in Cp rings); FTIR (film): ν (cm^{-1}): 436–556 (Fe-Cp), 1082–1225 (C–O stretching vibration), 3299–3662 (–N–H stretching vibration), 1133 (C–N stretching vibration), 3074–3149 (═C–H).

2.3.5 Synthesis of Schiff base linked DOX prodrug $(DOX)_2$–Cys–$(PEG_{45})_2$-*b*-$(PMAOEFC)_2$. The prodrug $(DOX)_2$–Cys–$(PEG_{45})_2$-*b*-$(PMAOEFC)_2$ was fabricated through Schiff base linking between DOX and Cys–$(PEG_{45})_2$-*b*-$(PMAOEFC)_2$ backbone. Specifically, Cys–$(PEG_{45})_2$-*b*-$(PMAOEFC)_2$ (205 mg, 8.7×10^{-3} mmol) was dissolved in anhydrous DMF (20 mL), then DOX·HCl (252 mg, 0.435 mmol) and TEA (60.3 μL, 0.435 mmol) solution in dessicated DMF (10 mL) was dropwise added into the above solution. The reaction was performed at 25 °C for 48 h in the presence of nitrogen, $(DOX)_2$–Cys–$(PEG_{45})_2$-*b*-$(PMAOEFC)_2$ was isolated by extensive dialysis, followed by freeze drying, and denoted as P-DOX thereinafter. (Yield: 91%) (^{1}H NMR: 300 MHz, $CDCl_3$), δ (ppm): 7.48–8.09 (aromatic protons in DOX), 4.18 (5H in ferrocenyl protons), 4.36 (2H, s, *meta*-H in Cp rings), 4.80 (2H, s, *ortho*-H in Cp rings), 3.51 (–O$\underline{CH_2}\underline{CH_2}$O– in PEG2000); FTIR (film): ν (cm^{-1}): 3013–3149 (═C–H and aromatic –C–H stretching vibration), 1720 (–C═O), 427–527 (Fe-Cp), 1574 (benzene skeleton vibration), 1613 (–C═N).

2.4 Preparation of nanomicelles

Polymeric micelles were prepared by dialysis method in aqueous solution, briefly, polymer P powder (20 mg) was dissolved in DMF (10 mL) with stirring at 25 °C, followed by extensive dialysis (MWCO = 8000) against deionized water for 72 h till the solution became opaque. Thus, the polymeric micellar solution with the origin concentration of 2000 mg L^{-1} was collected in a 10 mL volumetric flask for further measurements. The P-DOX micelles were prepared in line with the same procedure as the above.

2.5 Characterization

^{1}H NMR spectra of products were recorded on a 400 MHz Bruker Avance spectrometer (Bruker, Germany) at 25 °C serving tetramethylsilane (TMS) as internal standard and $CDCl_3$, DMSO-d_6 as solvent, respectively. Fourier transform infrared (FTIR) spectra were detected by an EQUINX55 FTIR spectrophotometer (Bruker Corp., Germany) in KBr squash method. The molecular weight and polydispersity index (PDI) of products were measured using a gel permeation chromatography (GPC, Waters Corp., USA) system equipped with Waters 515 pump and 2410 differential refractive index detector, and linear polystyrene was used as calibrated standards. Chromatographically pure THF was served as eluent at flow rate of 1 mL min^{-1}.

The critical micelle concentration (CMC) is a representative measurement for self-assembly behavior investigation, which was performed on a FluoroMax-4 spectrofluorophotometer (HORIBA Scientific, America) employing pyrene as probe. Specifically, 4.8 μL of pyrene–acetone solution (5×10^{-4} M) was added in sample tube, and dried to remove solvent completely, followed by adding the micelles with the concentration from 5×10^{-4} to 1 mg mL^{-1} into the corresponding tube under stirring overnight. The spectroscopy was recorded under the condition of the excitation wavelength at 330, and the emission wavelength ranged 350–500 nm, respectively, All the slit width was 2 nm. The CMC value was calculated from the intersection of two tangents according to the fitted curves of the ratio of fluorescence intensity I_{383}/I_{372} *versus* the logarithm of micellar concentration ($\log C$).

The hydrodynamic diameter (D_h) and polydispersity index (PDI) of the fresh micelles (500 mg L^{-1}) were monitored by a dynamic light scattering (DLS, BI-90Plus, USA) instrument. To further observe the micellar morphologies and size dispersity, a JEM-2100 transmission electron microscopy (TEM, ElectronCrop., Japan) was applied to capture micellar photographs at an accelerating voltage of 200 keV. The samples were prepared by transferring 10 μL of micellar solution dropped on carbon films, followed by air-drying to ensure the moisture removed completely.

The ultraviolet-visible (UV-vis) absorption spectra of micellar solution were recorded on an UV-vis spectrophotometer (UV-6100S, Mapada, Shanghai).

CV detection was performed on a CHI 660E electrochemical workstation (Shanghai Chenhua Instrument Co., China) with a conventional three-electrode cell in 0.1M TBAHFP electrolyte at a scan rate of 1–50 mV s^{-1} to investigate the electrochemical property of monomer MAOEFC and polymer, glassy carbon electrode (GCE), saturated calomel electrode and platinum wire electrode were served as working electrode, reference electrode and counter electrode, respectively.

2.6 Formation of PTX laden micelles

PTX was entrapped into polymer P through the hydrophobic interactions, π–π stacking and hydrogen bonding between PMAOEFC and drugs. Specifically, P powder (30 mg) and PTX (10 mg) were dissolved in DMF (10 mL) with stirring overnight, then extensive dialysis (MWCO = 3500 Da) was performed against deionized water for 72 h to remove solvent. The unloaded PTX was removed through low speed centrifugation, followed by lyophilization to obtain PTX laden P micelles (denote as $P^{@PTX}$ hereafter). Similarly, PTX laden P-DOX, diselenide bond linked PTX dimer (PTX–SeSe–PTX, signify as PTX dimer, the synthetic details were presented in ESI†) laden P-DOX micelles were formed in accordance with the above method,

which were represented as P-DOX$^{@PTX}$ and P-DOX$^{@PTX\,dimer}$, respectively.

The drug laden micelles were dissolved in DMF to estimate the drug loading content (DLC) and drug encapsulation efficiency (DEE) in light of the following equations:

$$\text{DLC (\%)} = [\text{mass of PTX (dimer) in PTX laden micelles/mass of PTX (dimer) laden micelles}] \times 100\% \quad (1)$$

$$\text{DEE (\%)} = [\text{mass of PTX (dimer) in PTX laden micelles/mass of PTX (dimer) added initially}] \times 100\% \quad (2)$$

The calibration equation of free PTX was obtained by the relation between the concentration of PTX–DMF standard solution and their corresponding UV-vis absorption, which was presented as the following formula:

$$C\ (\text{mg L}^{-1}) = (A - 0.0128)/0.39082\ (R^2 = 0.9982) \quad (3)$$

where C and A is the concentration and UV absorbance at 210 nm of PTX–DMF standard solution, respectively.

Similarly, the calibration equation of free DOX–DMSO solution was fitted according to the same way, as shown below:

$$C\ (\text{mg L}^{-1}) = (A + 0.03737)/0.01882\ (R^2 = 0.9949) \quad (4)$$

where C and A denote the concentration and UV-vis absorbance at 480 nm of DOX–DMSO standard solution, separately.

2.7 Redox responsiveness of the micelles

The redox responsive property of micelles was studies by DLS, TEM and UV-vis spectrometer under specific conditions. To investigate oxidization behavior, 0.1 mL of 1.5, 5.0, 7.5% NaClO and 0.2 mL of H_2O_2 with the same mass concentrations were blended into each 5 mL of micellar solution, successively. The resulting solution was agitated for 4 h at 25 °C. Afterwards, 0.1 mL of 0.1 M Vc solution was added into the corresponding oxidized micellar solution by 7.5% NaClO and 7.5% H_2O_2 with stirring for 4 h respectively. To obtain reduced micelles, GSH (12.3 mg) was added into 4 mL of the prepared micellar solutions with agitation at 25 °C for 2, 6, 24 and 48 h.

2.8 pH responsiveness of P-DOX micelles

The measurements of ^{1}H NMR, fluorescence spectroscopy and D_h of P-DOX micelles containing Schiff base structure were performed to monitor the pH responsiveness. The P-DOX lyophilized micelles (60 mg) was dissolved in DMSO (10 mg mL^{-1}) entirely, and divided into two groups, then 1 mL of pH 5.0 and isometric pH 7.4 PBS were mixed into their corresponding groups under stirring for 24 h, respectively. The resulting liquor was vacuum dried and redissolved in DMSO-d_6 for ^{1}H NMR determination.

The detection of micellar size (D_h) changes and DOX fluorescence intensity after DOX cleaving from P-DOX micelles in weak acidic environment within different time intervals using DLS and fluorescence spectrophotometer, respectively. Lyophilized P-DOX micelles was dissolved in pH 5.0 and pH 7.4 PBS at the concentration of 0.5 mg mL^{-1} and detect the D_h every 10 min within 1 h. And the fluorescence emission spectroscopy ranged from 525 to 700 nm was collected within 90 min when the excitation wavelength was 469 nm, and all slit width was 5 nm.

Furthermore, *in vitro* DOX release experiments of P-DOX micelles were administrated to detect pH sensitivity quantitatively. The lyophilized P-DOX micelles (4 mg) were suspended in pH 5.0 and 7.4 PBS at the concentration of 1.0 mg mL^{-1} and shifted in dialysis bag (MWCO = 3500 Da), then dipped in a beaker containing 200 mL of the corresponding pH value PBS at 37 °C with gentle stirring (stirring rate: 100 rpm). At predetermined time intervals within 60 h, 4 mL of outer medium was extracted and supplemented with isometric fresh medium. The concentration of DOX released was detected using UV-vis spectrophotometer at 480 nm, and calculated *via* the calibration eqn (4) to assess the cumulative DOX release amount.

2.9 Stimuli induced *in vitro* drug release

Stimuli triggered PTX and DOX release behavior was investigated by dialysis method. 4 mL of drug contained micelles solution (1 mg mL^{-1}) was encased in dialysis tube (MWCO = 5 kDa) and extensive dialyzed against 200 mL of pH 5.0 PBS with 10 mM GSH/100 μM H_2O_2/0.5% NaClO at 39 °C for 60 h, respectively. 4 mL of outer medium was extracted at specific time points and replenished with isometric fresh medium to detect the cumulative amount of drugs released. The same release procedure was performed in pH 7.4 PBS at 37 °C for 60 h.

2.10 *In vitro* cytotoxicity

The mouse fibroblast cell line L929 and HeLa cell line were respectively selected as representatives of normal and tumor cells for assessing the cytotoxicity of the prepared micelles. The cells were seeded in 96-well at the density of 5×10^3 cells per well and incubated in DMEM containing 10% FBS for 24 h, followed by the medium removal, cells were rinsed using PBS and fresh medium supplementation. The HeLa cells were treated with the 0.1–16 mg L^{-1} of free drugs (PTX and DOX·HCl), 0.1–500 mg L^{-1} of the P, P$^{@PTX}$, P-DOX, P-DOX$^{@PTX}$, P-DOX$^{@PTX\,dimer}$ micellar solution were used for culturing L929 and HeLa cells. After 48 h, the medium was discarded and added another 200 μL fresh medium containing 20 μL MTT solution (5 mg mL^{-1}), followed by incubation at 37 °C for 4 h. 150 μL of DMSO was used to dissolve formazan with shaking for 10 min. The optical density (OD) was recorded on an universal microplate reader (Model 680, UK) at 570 nm. As control, HeLa cells were cultured under the same condition without any drug and nanoformula addition. Cell viability was calculated according to the following equation:

$$\text{Cell viability (\%)} = \text{OD}_{\text{sample}}/\text{OD}_{\text{control}} \times 100\% \quad (5)$$

where the $\text{OD}_{\text{sample}}$ and $\text{OD}_{\text{control}}$ represent the optical density of samples and control group, respectively.

2.11 Apoptosis analysis

To observe the uptake of DOX into cells, HCT116 and HCT116/ADR cells were seeded in 6-well plates with cell slides (1 × 105 cells per

well) and incubated for 24 h. Then the cells were washed with PBS and cultured with a medium containing free DOX, P-DOX, P-DOX$^{@PTX}$ and P-DOX$^{@PTX\,dimer}$ at 1 μg mL^{-1} DOX concentration for 4 h, respectively. RPMI1640 treated cells as a control group. After that, the cells were washed using PBS and digested using trypsin, followed by resuspension in buffer and staining with Annexin V-FITC and propidium iodide (PI). The growth inhibition caused by the above nanoformulations was detected by flow cytometry.

2.12 Qualitative and quantitative analysis of cellular uptake

To quantitative analysis the celluar uptake of free DOX, P-DOX, P-DOX$^{@PTX}$ and P-DOX$^{@PTX\,dimer}$, HCT116 and HCT116/ADR cells were seeded in 6-well plate with a cover slip (1×10^5 cells per well) and cultured for 24 h. After removing the old medium, the cells were cultured with new medium containing samples at 2 μg mL^{-1} DOX concentration for 1 and 4 h. Then the cells were fixed using 4% paraformaldehyde and washed with PBS thrice. The cytoskeleton was labled with 50 nM phalloidin-FITC, similarly, nucleus were stained with 300 nM 4-, 6-diamidino-2 phenylindole (DAPI) and observed through confocal laser scanning microscope (CLSM, Nikon A1, Japan).

Flow cytometer was used to quantitatively analyze intracellular drugs content. The HCT116and HCT116/ADR cells cultured with DOX and all nanoformulations for 4 h. RPMI1640 treated cells as a control group. Afterwards, cells were washed with PBS thrice, digested using trypsin solution, centrifuged and collected cells. The intracellular fluorescence intensity of DOX was determined using flow cytometry.''

2.13 *In vivo* anticancer study

4T1 tumor bearing Balb/c mice were treated using DOX·HCl, PTX, P, P-DOX, P-DOX$^{@PTX}$ and P-DOX$^{@PTX\,dimer}$ micellar solutions at PTX and DOX dosage of 8 and 4 mg kg^{-1}, respectively, PBS treated group was served as blank control group. All nanoformulas were injected every three days. 4T1 tumor volumes (V) were measured using caliper on day 0, 3, 6, 9, 12, 15, and mice were weighed at the same time intervals. Tumor suppression ratio (TSR%) = $[(V_{PBS} - V_{NF})/V_{PBS}] \times 100\%$ (here V_{PBS} and V_{NF} denote the 4T1 tumor volume treated by PBS and nanoformula, respectively).

2.14 Histological analysis

On day 15, one mouse from each cohort was sacrificed to excise the major organs (heart, liver, spleen, lung and kidney). After immersion in paraformaldehyde and embedding in paraffin, the organs were sliced into 5 μm sheets. The obtained slices were stained with hematoxylic and eosin (H&E) for further observation under digital microscope (Leica QWin).

2.15 Statistical analysis

The results of drug release, *in vitro* cytotoxicity, and *in vivo* antitumor experiments have been denoted as the average ± standard deviation (average ± S.D.), tests were carried out quantitative, and taken the average values. The significance of any couples of differences was affirmed through Statistical Product and Service Solutions (SPSS). *, # and & signify $P < 0.05$, $P < 0.01$ and $P < 0.001$, respectively.

3. Results and discussion

3.1 Synthesis of DOX prodrug P-DOX

Schiff base linked DOX prodrug P-DOX was prepared through the following five-step process: (i) esterification between (Boc–Cys–OH)$_2$ and PEG; (ii) acylbromination of (Boc)$_2$–Cys–(PEG$_{45}$)$_2$ affording macromolecular initiator (Boc)$_2$–Cys–(PEG$_{45}$)$_2$–Br$_2$; (iii) ATRP of monomer MAOEFC yielding (Boc)$_2$–Cys–(PEG$_{45}$)$_2$-*b*-(PMAOEFC)$_2$; (iv) de-protection of (Boc)$_2$–Cys–(PEG$_{45}$)$_2$-*b*-(PMAOEFC)$_2$ and (v) conjugation of DOX with P resulting P-DOX. ^{1}H NMR was applied to confirm the chemical structure of products, as demonstrated in Fig. 1. The chemical signal of methylene in PEG appears at 3.65 ppm in Fig. 1A, by contrast, a new signal shows at 1.87 ppm belonging to methyl from BiBB residues in Fig. 1B. After polymerization, ^{1}H NMR spectrum of (Boc)$_2$–Cys–(PEG$_{45}$)$_2$-*b*-(PMAOEFC)$_2$ not only presents peaks at 1.68 and 1.09 ppm assigned to methylene and methyl in PMAOEFC main chains respectively, but also shows the chemical shifts of ferrocenyl protons, *meta*-H and *ortho*-H emerge at 4.04, 4.20 and 4.80 ppm, successively, see in Fig. 1C. The characteristic signal of *t*-butyl at 1.43 ppm disappears after de-protection, as exhibited in Fig. 1D. In addition, as shown in Fig. 1E and F, new peaks display at 7.48–8.09 ppm are the characteristic signal of aromatic protons in DOX structure, indicating the formation of P-DOX with Schiff base structure. FTIR was employed to further confirm the chemical structure of products in Fig. 2A.

In Fig. 2A(a), the strong vibration bands located at 1007–1214, 2848–2981 and 3080–3755 cm^{-1} are attributed to asymmetric C–O–C, –C–H stretching vibration in PEG and terminated –OH from (Boc)$_2$–Cys–(PEG$_{45}$)$_2$, respectively. For (Boc)$_2$–Cys–(PEG$_{45}$)$_2$-*b*-(PMAOEFC)$_2$, the absorption peak of ═C–H, ═C–H in ferrocene rings and Fe–C/C$_p$–Fe emerge at 3100, 770–850 and 427–563 cm^{-1}, as demonstrated in Fig. 2A(b). After de-protection, it can be seen that –N–H and –C–N stretching vibration bands are located at 3229–3662 and 1133 cm^{-1}, respectively, demonstrating the generation of polymer P. In addition to the tagged spectral features of PMAOEFC and PEG appearing in Fig. 2A(d), some new wide peaks also appear at 3013–3149, 1574 and 1613 cm^{-1}, which are attributable to unsaturated –C═H stretching vibration, benzene ring skeleton stretching vibration and –C═N– in P-DOX.

The experimental molecular weight of (Boc)$_2$–Cys–(PEG$_{45}$)$_2$-*b*-(PMAOEFC)$_2$ was assessed using integration area ratio of *t*-butyl peak in Boc group at 1.45 ppm to the shift of *ortho*-H from PMAOEFC block at 4.80 ppm. There are approximately 56 MAOEFC repeating units polymerized in (Boc)$_2$–Cys–(PEG$_{45}$)$_2$-*b*-(PMAOEFC)$_2$, *viz.*, the composition can be denoted as (Boc)$_2$–Cys–(PEG$_{45}$)$_2$-*b*-(PMAOEFC$_{28}$)$_2$. The apparent molecular weight (M_n, M_w) and polydispersity index (PDI, M_w/M_n) of all polymers were also determined through GPC, the obtained GPC trace is displayed in Fig. 2B and the molecular weight was shown in

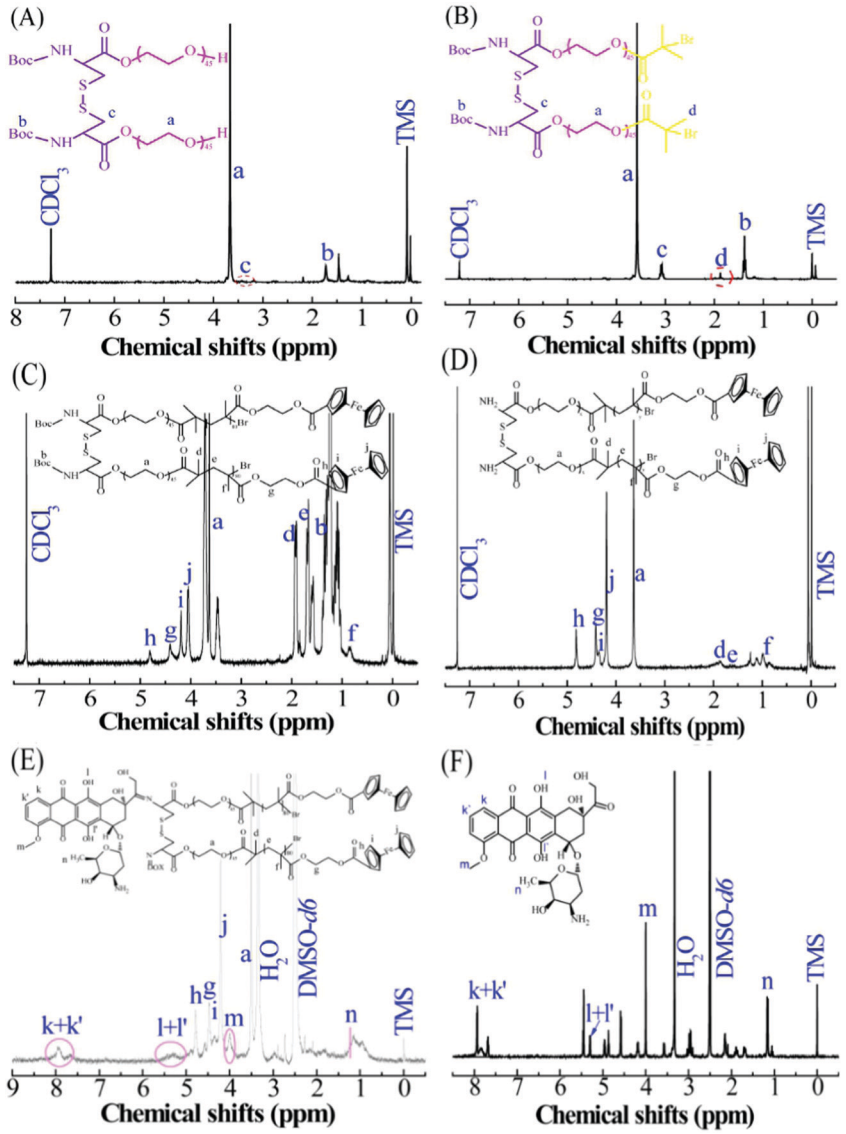

Fig. 1 ^{1}H NMR spectra of $(Boc)_2$–Cys–$(PEG_{45})_2$ (A), $(Boc)_2$–Cys–$(PEG_{45})_2$–Br_2 (B), $(Boc)_2$–Cys–$(PEG_{45})_2$-*b*-$(PMAOEFC)_2$ (C), polymer P (D), P-DOX (E) and DOX·HCl (F).

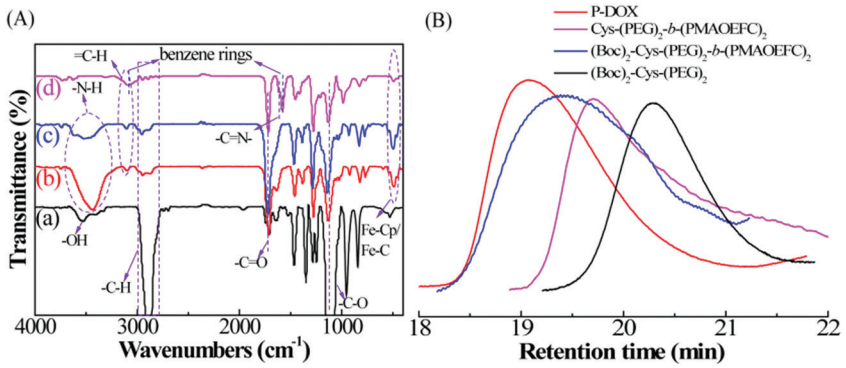

Fig. 2 FTIR spectra (A) of $(Boc)_2$–Cys–$(PEG_{45})_2$ (a), $(Boc)_2$–Cys–$(PEG_{45})_2$-*b*-$(PMAOEFC)_2$ (b), polymer P (c) and P-DOX (d); (B) GPC trace of all polymers.

Table 1. Obviously, there is no tailing and shoulder peak in symmetric GPC trace during the whole retention region of molecular weight, suggesting that the polymers have well control and satisfactory purification over synthesis process.

Table 1 Molecular weight of polymers from GPC

	Name	M_w	M_n	PDI (M_w/M_n)
$(Boc)_2$–Cys–$(PEG)_2$	—	17 893	16 018	1.117
$(Boc)_2$–Cys–$(PEG)_2$-*b*-$(PMAOEFC)_2$	—	88 410	56 384	1.568
Cys–$(PEG)_2$-*b*-$(PMAOEFC)_2$	P	67 322	48 784	1.380
$(DOX)_2$–Cys–$(PEG)_2$-*b*-$(PMAOEFC)_2$	P-DOX	70 410	66 910	1.052

All polymers possess reasonable molecular weight and uniform molecular weight dispersion.

3.2 Self-assembly behavior in aqueous solution

As illustrated in Scheme 2, micelles were prepared using dialysis method. Fluorescence spectroscopy, DLS and TEM were used to study the micellization behavior. The CMC assessed in the presence of pyrene probe was showed in Fig. 3A, suggesting that P-DOX$^{@PTX\,dimer}$ micelles possess the minimum CMC of 5.78 mg mL^{-1} compared that of other prepared micelles (238.93 mg mL^{-1} for P micelles, 12.09 and 12.07 mg mL^{-1} for P-DOX and P-DOX$^{@PTX}$ micelles). This could be attributed to the abundant drug types and highest drug content of P-DOX$^{@PTX\,dimer}$ micelles, the enhanced hydrophobicity from π–π stacking, hydrophobic interaction, hydrogen bond interaction of among PMAOEFC, PTX and DOX, which caused a more stable micelle.[45,46] The limited amount of DOX contained in P-DOX micelles can improve stability compared with that of P micelles. The sharp decrease of CMC shows that P-DOX, P-DOX$^{@PTX}$ and P-DOX$^{@PTX\,dimer}$ micelles can withstand the dilution of body liquids during blood circulation. Thus, they have the potential to be applied in cancer treatment.[47,48] The monodisperse trend exhibited in Fig. 3B shows the average D_h of 151.7, 383, 443.8, 422.9 nm and PDI of 0.297, 0.336, 0.363, 0.285 for P, P-DOX, P-DOX$^{@PTX}$ and P-DOX$^{@PTX\,dimer}$ micelles, successively, somewhat larger than micellar size from TEM, as displayed in Fig. 3C–F, which is mainly ascribed to the dehydration process before TEM observation. The P-DOX, P-DOX$^{@PTX}$ and P-DOX$^{@PTX\,dimer}$ formed globular core–shell micellar aggregates with average size of 200, 220 and 235 nm compared to 138 nm for P micelles. All the prepared micelles are of homogenous dispersion as PDI results from Fig. 3B. As drugs were introduced into P-DOX, P-DOX$^{@PTX}$ and P-DOX$^{@PTX\,dimer}$ micelles, the enhanced hydrophobic interaction and expanded core volumes lead to the larger micelles aggregates formed.

3.3 Redox responsiveness of PEG based polymer P micelles

Based on the existence of redox sensitive ferrocene in Polymer P micelles, it was selected to investigate redox behavior of P. Apart from H_2O_2, moreover, NaClO also can oxidize PMAOEFC into poly(ferrocenium), their redox responsiveness was monitored through UV-vis spectroscopy. As shown in Fig. 4, the UV-vis absorption peak of PMAOEFC in a reduction state appears approximately at 450 nm. The peak is weak or fades away after blending oxidants (H_2O_2 and NaClO) with the mass concentration of 1.5%, 5.0% and 7.5%. Upon H_2O_2 addition, as illustrated in Fig. 4A, the peak at 450 nm of ferrocene is almost fades away at the H_2O_2 concentration of 5.0% due to the formation of poly(ferrocenium). The oxidization mechanism involved is the production of unstable intermediates hydroperoxide anions HOO^-, which is subsequently decomposed to $HO^{\bullet}$.[49] With respect to NaClO, the characteristic peak decreases with the increasing concentration of NaClO in Fig. 4B. It is noteworthy that the hydrolysate of NaClO solution containing NaOH and HClO can destroy micelles, resulting in the oxidation and aggregation of micelles.[50]

As a reductant, Vc was added in the oxidized micellar solution to reduce the poly(ferrocenium), the characteristic peak at 450 nm is reemerged, which is ascribed to the transition of Cp_2Fe^+ to Cp_2Fe under reduced condition. These results suggest the reversibility of redox-triggered assembly and disassembly behavior.[16,51] Furthermore, the smart responsive

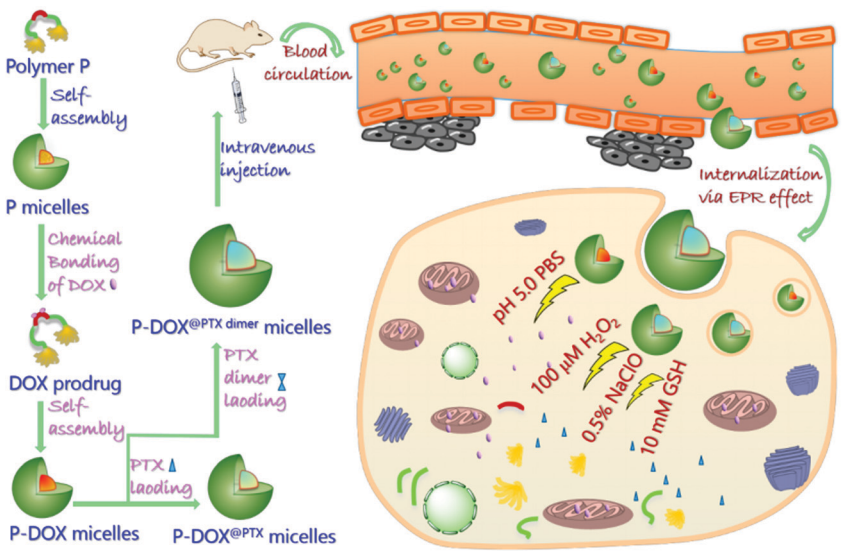

Scheme 2 Schematic illustration of preparation, blood circulation, internalization, specific drug release of P-DOX, P-DOX$^{@PTX}$ and P-DOX$^{@PTX\,dimer}$ micelles.

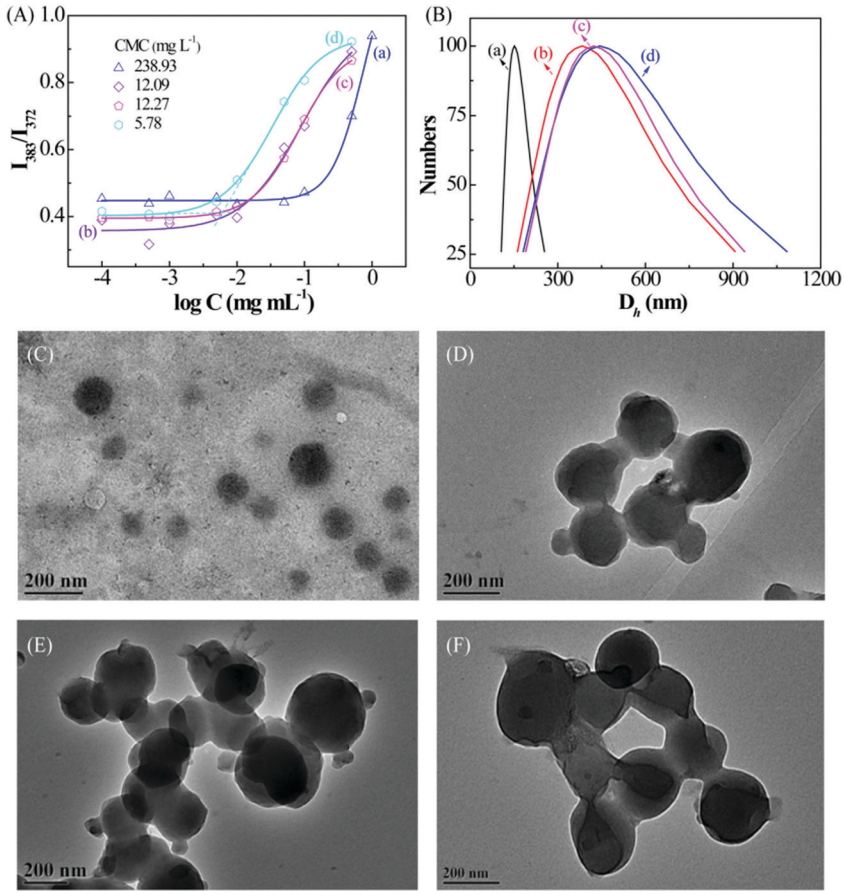

Fig. 3 (A) The fluorescence intensity ratio (I_{383}/I_{372}) *versus* the logarithm of P (a), P-DOX (b), P-DOX$^{@PTX}$ (c) and P-DOX$^{@PTX\,dimer}$ (d) micellar concentrations; (B) particle size dispersion of P (a), P-DOX (b), P-DOX$^{@PTX}$ (c), P-DOX$^{@PTX\,dimer}$ (d) micelles; TEM photos of P (C), P-DOX (D), P-DOX$^{@PTX}$ (E) and P-DOX$^{@PTX\,dimer}$ (F) micelles.

behavior to redox is expected to be a new channel for intelligent drug delivery.[51–53]

3.4 Electrochemical responsiveness of PEG based polymer P

The redox responsiveness was studied using cyclic voltammetry (CV). As exhibited in Fig. 4C, the ferrocene content affects the redox potential directly. The anodic oxidation potential of monomer MAOEFC is 0.865 V, in case of polymer P, the presence of cystine and PEG lead to the anodic oxidation potential reduce to 0.849 V. Additionally, the potential difference between anodes and cathodes was considered as the peak separation ΔE ($\Delta E = E_{P,anodic} - E_{P,cathodic}$), the sample containing ferrocene has a good redox reversibility when ΔE is less than 0.1 V. Compared with ΔE of ferrocene monomer (0.030 V), ΔE of P reached 0.157 V due to more MAOEFC repeating units oxidized and the resulting MAOEFC$^+$ segments reduced in electrolyte, reflecting that P is more difficult to be oxidized. In fact, the increase of ΔE is attributable to high ferrocene contents which result in mass diffusion and charge transfer at a lower speed. Therefore, the reversibility of P can be adjusted by decreasing the concentration less than 10 mg mL^{-1} and $\Delta E < 0.1$ V.

The electrode process mechanism of P was also uncovered by CV in DCM containing 0.1 M TBAHFP at the scan rates ranged from 1 to 50 mV s^{-1}, the results are shown in Fig. 4D. The oxidation of MAOEFC segments and the reduction of MAOEFC$^+$ occurred in each scanning process at different scan rate, the peak potential ΔE is increase due to scanning speed up, which results in a weaken reversibility. To further reveal electrode process mechanism, the relationship between the peak currents (I_p) and the square root of their corresponding scan rate ($\nu^{1/2}$) was fitted in the inset of Fig. 4D. The I_p is proportional to $\nu^{1/2}$, taking on good linear relations $I_{p,a} = 0.49371\nu^{1/2} - 2.14902$ (R^2 = 0.95125) for anode and $I_{p,c} = -0.62037\nu^{1/2} + 2.7336$ (R^2 = 0.9744) for cathode, respectively, which signify that the mass diffusion of oxidation and reduction is adjustable, and the electron transfer process is sufficient to oxidize and reduce the whole MAOEFC units from P in electrolyte. In fact, the diffusion controlled redox electrode process also can be deduced from Fig. 4D, where the ΔE enhanced as $\nu^{1/2}$ increasing. The result is probably ascribed to the slow electron transfer process at the electrode–P interface in electrolyte solution and even between contiguous ferrocene units.[54]

3.5 pH responsiveness of P-DOX micelles with Schiff base structure

Schiff base structure can be maintained under normal physiological environments (pH 7.4), but it can be cracked into amino, aldehyde, and ketone under low pH condition (~pH 5.0), the mechanism is

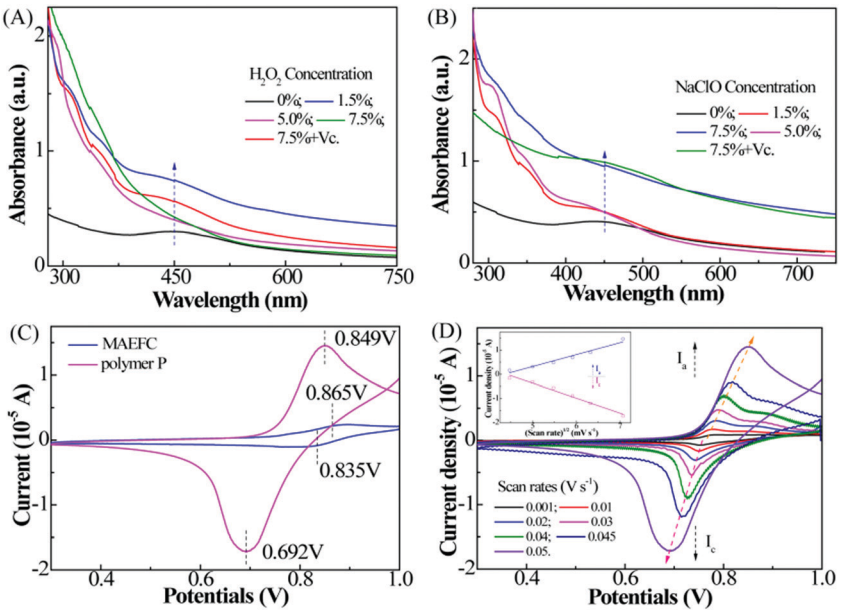

Fig. 4 UV-vis spectra of P micellar aqueous solution before and after oxidization through (A) H_2O_2 and (B) NaClO with the mass concentration from 0–7.5%, followed by Vc reduction. Cyclic voltammograms of monomer MAOEFC and polymer P with a concentration of 10 mg mL^{-1} in DCM containing 0.1 M TBAHFP at a scan rate of 50 mV s^{-1} (C), cyclic voltammograms (D) and linear relations (the inset) of peak current I_p *versus* the square root of scan rates of P (10 mg mL^{-1}) at different scan rates ranged 1–50 mV s^{-1} in the same electrolyte at room temperature.

exhibited in Fig. 5A.[55,56] According to ^{1}H NMR, DLS and fluorescence spectrophotometry, the results are shown in Fig. 5B–F. In terms of P-DOX, Schiff base structure was destroyed and the fluorescent DOX disengaged from P-DOX micelles at pH 5.0, causing the fluorescence intensity increased and micellar diameter decreased. As shown in Fig. 5B, with the induction of weak acidic ambient, more free DOX was released after Schiff base structure was destructed and produced the stronger fluorescence. By contrast, the limited florescence intensity increased in Fig. 5C, which was up to the less DOX separation and the better stability of P-DOX in pH 7.4 PBS compared with that in pH 5.0 PBS. Similarly, as shown in Fig. 5D, D_h of P-DOX micelles was decreased from 516.7 nm to 330.3 nm after incubation in pH 5.0 PBS for 1 h, while a 50 nm of micellar size decreased in Fig. 5E when P-DOX micelles were immersed in pH 7.4 PBS. P-DOX was treated with pH 5.0 PBS and then dissolved in DMSO to monitor the acidic hydrolysis behavior of Schiff base using ^{1}H NMR. It is noteworthy that the chemical shifts of amino proton appear at approximately 2.0 ppm in Fig. 5F(a), and without specific chemical feature emerges in Fig. 5F(b) with respect to P-DOX micelles in pH 7.4 PBS. These evidence was further demonstrated that P-DOX micelles had pH triggered property under extracellular micro-environment in solid tumor,[57] especially in endosomes and lysosomes of tumor tissue.[58–60]

3.6 Redox and pH-triggered properties of P-DOX$^{@PTX\ dimer}$ micelles

In view of the presence of the multiple redox sensitive sites including diselenide bond, disulfide bond and PMAOEFC blocks in P-DOX$^{@PTX\ dimer}$ micelles, TEM was selected to observe the changes of morphology and micellar size of P-DOX$^{@PTX\ dimer}$ micelles under various of mimic cancerous physiological conditions such as 10 mM GSH, 100 μM H_2O_2 and pH 5.0 PBS. As observed in Fig. 6A, the mean diameter of P-DOX$^{@PTX\ dimer}$ micelles has a sharply decrease from 235 to 141 nm after incubation in 10 mM GSH for 24 h, which was caused by the reduction of diselenium and disulfide bond into the enhanced hydrophilic selenol and mercaptan, respectively, and the follow-up micellar disassembly. Thus, D_h firstly increased and then decreased. Besides, diselenide bonds were oxidized into selenic acid by 100 μM H_2O_2, meanwhile, Cp_2Fe^+ was also generated after Cp_2Fe oxidation. The micellar size of the oxidized micelles from 285 to 457 nm (average D_h: 395 nm) in Fig. 6B was ascribed to the electrostatic repulsion between Cp_2Fe^+ units and the swelling effect of the resulting hydrophilic poly(ferrcenium).[61] In addition, the oxidation of PMAOEFC is a relatively slow process, and most of PTX still remain in carrier.[60] Therefore, the increase of micellar size is depended on the synergistic effect of swelling, electrostatic repulsion and drugs residues. There were some debris on micellar surface showed in Fig. 6B, clearly suggested the oxidation of micelles. These results were consistent with the D_h change trends of the P-DOX$^{@PTX\ dimer}$ micelles within different reduction and oxidization time intervals in Fig. S4 (ESI†). The disassembly performance of P-DOX$^{@PTX\ dimer}$ micelles was reflected by DOX release under weak acidic condition (pH 5.0 PBS) after 60 h shown in Fig. 6C, innumerable spots with approximately 18 nm of average diameter appeared on the surface of hollow micelles with the size of 363 nm, which precisely indicated that DOX was disconnected from P-DOX$^{@PTX\ dimer}$ micelles after Schiff base structure destruction under pH 5.0 PBS. The empty core was formed when Schiff base linkage cleaved and the DOX diffused, which can attest the pH responsiveness of P-DOX$^{@PTX\ dimer}$ micelles. It is noticeable that the P-DOX$^{@PTX\ dimer}$ micelles

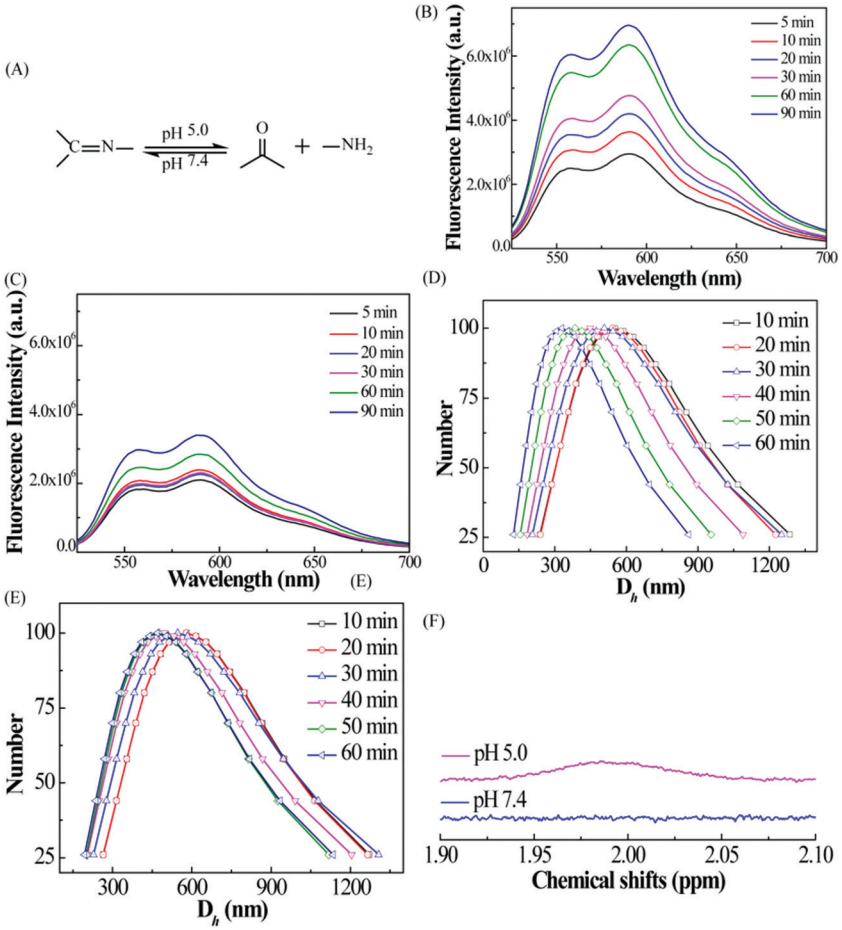

Fig. 5 Schematic of Schiff base hydrolytic process (A); fluorescence spectra of P-DOX micelles treated with pH 5.0 PBS (B) and pH 7.4 PBS (C); micellar size dispersion of P-DOX after incubation with pH 5.0 PBS (D) and pH 7.4 PBS (E) at different time intervals; ^{1}H NMR spectra of P-DOX after pH 5.0 and 7.4 PBS treatment (F).

was dissociated entirely under the condition of pH 5.0 PBS containing 10 mM GSH, this is mainly due to the reduction of diselenide and disulfide bonds located in micellar core region, leading to the formation of PTX unimers, and PTX and DOX release afterwards. As displayed in Fig. 6D, the intrinsic morphology of P-DOX$^{@PTX\,dimer}$ micelles disappeared completely and reversely replaced by spherical nanoparticles of free drugs with the D_h of approximately 7–23 nm.

3.7 Drug encapsulation

DOX and PTX were used as template drugs to construct dual drugs co-delivery system. As presented in Table 2, DOX was linked with P scaffold by Schiff base structure, affording P-DOX micelles with 39.3% of DOX content. This value was higher than 15.8% of DOX content calculated from feed molar ratio in line with reaction formula, which was due to both strong hydrophobic, hydrogen bond and π–π stacking interactions in DOX moieties. For comparison, polymer P, as a carrier to load PTX mainly through hydrophobic interaction with PMAOEFC segments, produced a single PTX delivery system P$^{@PTX}$ containing 12.7% of PTX. Even so, low drug content and single drug type were still existed in P and P$^{@PTX}$ system. To enrich drugs variety, improve drug delivery process and therapeutic effect, and circumvent MDR effect, PTX and its diselenide bond linked dimer PTX–SeSe–PTX were encapsulated into P-DOX in the same way, obtaining the dual drugs co-delivery systems P-DOX$^{@PTX}$ (13.2% of LC, 57.0% of EE) and P-DOX$^{@PTX\,dimer}$ (49.1% of LC, 97.0% of EE), respectively. In particular, more PTX was pulled in P-DOX by diselenide bond, leading to enhanced hydrophobic interaction with DOX and PMOAEFC blocks. Above all, diselenide bonds were used as highly entangled networks convolve the micellar core comprised of DOX, PMAOEFC and large amount of PTX, which could avoid the pre-leak of drugs before reaching tumor site. Together with 39.3% of DOX, the total content of dual drugs in P-DOX$^{@PTX\,dimer}$ had up to 88.4%. DOX and PTX dual drugs co-delivery systems with favorable loading performance were prepared hereto, indicating that the variety of nanocarriers can be enriched by choosing chemical bonding/physical encapsulation and loading drug unimer/dimer delivery.[59]

3.8 pH, redox triggered *in vitro* drug release

Due to the abundant drugs containing in P-DOX$^{@PTX\,dimer}$ micelles, *in vitro* drug release behaviors are shown in Fig. 7.

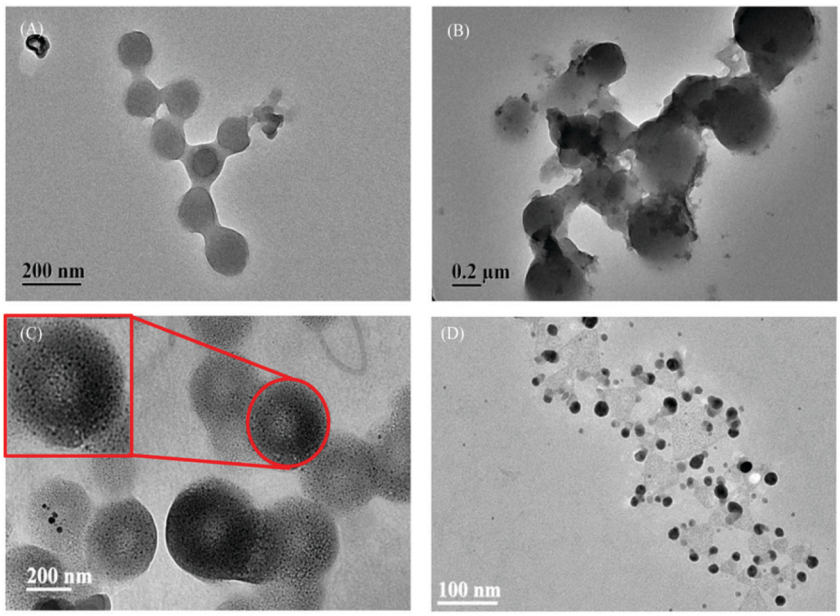

Fig. 6 TEM photographs of P-DOX$^{@PTX\,dimer}$ micelles reduced by 10 mM GSH for 24 h (A), oxidized by 100 μM H_2O_2 for 24 h (B), released in pH 5.0 PBS after 60 h (C) and released in pH 5.0 PBS containing 10 mM GSH after 60 h (D). The inset shows the partial enlarged photograph of DOX released P-DOX$^{@PTX\,dimer}$ micelles.

Table 2 Chemical compositions, PTX LC, PTX EE and drug content of the resulting nanoformulas

Chemical compositions	Sample code	PTX LC (%)	PTX EE (%)	DOX content (%)	Drug total content (%)
$(DOX)_2$–Cys–$(PEG_{45})_2$-*b*-$(PMAOEFC_{28})_2$	P-DOX	0	0	39.3	39.3
Cys–$(PEG_{45})_2$-*b*-$(PMAOEFC_{28})_2$$^{@PTX}$	P$^{@PTX}$	12.7	48.9	0	12.7
$(DOX)_2$–Cys–$(PEG_{45})_2$-*b*-$(PMAOEFC_{28})_2$$^{@PTX}$	P-DOX$^{@PTX}$	13.2	57.0	39.3	52.5
$(DOX)_2$–Cys–$(PEG_{45})_2$-*b*-$(PMAOEFC_{28})_2$$^{@PTX\,dimer}$	P-DOX$^{@PTX\,dimer}$	49.1	97.0	39.3	88.4

Only 23.58% of PTX was released in pH 7.4 PBS from Fig. 7A(a), suggesting that the carrier could retard PTX release and avoid the side effects to normal tissues.

Unlike physical loading, 18.19% of DOX was disconnected from P-DOX$^{@PTX\,dimer}$ micelles, which was due to the good stability of chemical conjugate containing Schiff base structure at pH 7.4, as illustrated in Fig. 7B(a). Schiff base was hydrolysis under pH 5.0, resulting in 63.80% of DOX separated and diffused to micellar surface, as displayed in Fig. 7B(b) and C. Approximately 29.08% of PTX was released under the same condition regardless of acid labile mechanism, as shown in Fig. 7A(b). The diselenide and disulfide bond were reduced into selenol and mercaptan by 10 mM GSH, and the follow-up micellar disintegration. Eventually 72.65% of PTX was released from micelles in Fig. 7A(c), while DOX was not affected by GSH reduction, and 18.77% of DOX was detached from Fig. 7B(c). Besides, as exhibited in Fig. 7A(d), the release rate of PTX was controlled by the oxidation of diselenide bond and ferrocence based PMAOEFC blocks. Meanwhile, approximately 39.48% of PTX was released after incubation in medium containing 100 μM H_2O_2. It was apparent that the DOX release rate was essentially close to the amount released at pH 7.4. Indeed, it is difficult to obtain good release performance of dual drugs at the same time under a single stimulus. Remarkably, as illustrated in Fig. 7A(e), the PTX release amount was accumulated greatly into 84.04% under the synergistic reduction of disulfide and diselenide bonds for 60 h, while 71.97% of DOX released is mainly attributable to the pH 5.0 surrounding from Fig. 7B(e). Under the condition of pH 5.0 PBS containing 100 μM H_2O_2, PTX unimer and poly(ferrocenium) were formed and then occurred micellar phase transition, in which produced 42.28% of PTX was released, as shown in Fig. 7A(f). Compared with 63.80% of DOX released from P-DOX$^{@PTX\,dimer}$ micelles in pH 5.0 PBS, approximately 56.90% of DOX was released from the same carrier in pH 5.0 PBS containing 100 μM H_2O_2, which was ascribed to the limited diffused channels occupied by PTX, as shown in Fig. 7B(b) and (f). All these results suggested that the dual drugs carrier P-DOX$^{@PTX\,dimer}$ micelles can realize the appropriate drug release amount by controlling different response mechanisms. These prepared drug (co-)delivery systems with single, dual and even multiple stimuli responsiveness provide more choices for cancer treatment according to the required drug dosage,[16] especially the synergistic effects between pH and redox responsiveness of P-DOX$^{@PTX\,dimer}$ micelles can facilitate the drug accumulation with high concentration at tumor site.[59]

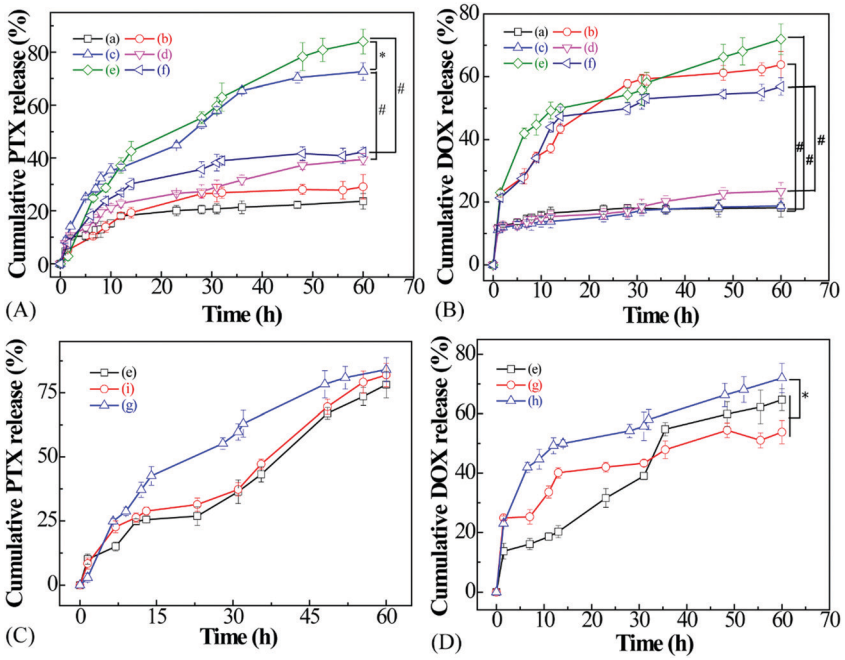

Fig. 7 PTX (A) and DOX (B) release plots of P-DOX$^{@PTX\,dimer}$ micelles in pH 7.4 PBS (a), pH 5.0 PBS (b), pH 7.4 PBS containing 10 mM GSH (c), pH 7.4 PBS containing 100 μM H_2O_2 (d), pH 5.0 PBS containing 10 mM GSH (e) and pH 5.0 PBS containing 100 μM H_2O_2 (f) for 60 h. PTX (C) release plots of P-DOX$^{@PTX\,dimer}$ (e), P-DOX$^{@PTX}$ (g) and P$^{@PTX}$ (i) micelles in pH 5.0 PBS containing 10 mM GSH for 60 h, DOX (D) release plots of P-DOX$^{@PTX\,dimer}$ (e), P-DOX$^{@PTX}$ (g) and P-DOX (h) micelles in pH 5.0 PBS containing 10 mM GSH for 60 h. $^{*}P < 0.05$ and $^{\#}P < 0.01$.

Due to the presence of hydrazone, disulfide and diselenide bonds in P-DOX$^{@PTX}$ micelles, approximately 81.28% of PTX released dramatically in pH 5.0 PBS containing 10 mM GSH was ascribed to simultaneous breakage of hydrazone, disulfide and diselenide bonds, as shown in Fig. 7C(e), while about 70.71% of DOX was isolated from P-DOX$^{@PTX\,dimer}$ as hydrazone bonds cracked in Fig. 7D(e). The similar PTX diffusion mechanism of P-DOX$^{@PTX}$ and P-DOX resulted in the analogue release trend in Fig. 7C(g) and Fig. 7C(i), and about 75% of PTX was disconnected from the two nanovehicles mentioned above. The steady release process of DOX occurred, as depicted in Fig. 7D(h), causing 48.92% of DOX dissociated. Actually, DOX and PTX competed to occupy the limited diffuse channels, thus a portion of DOX was bounded by PTX to release eventually, resulting in the amount of DOX released from P-DOX$^{@PTX\,dimer}$ surpassed that of DOX from P-DOX$^{@PTX}$, as revealed in Fig. 7D(e) and (g).

Owing to the unresponsiveness of hydrazone to pH 7.4 PBS, there was 9.11% of DOX released from P-DOX$^{@PTX}$ micelles, showing slightly less content of PTX released compared with P-DOX$^{@PTX\,dimer}$, that may be ascribed to a small number of PTX dragged by DOX through hydrophobic interaction and π–π stacking. As for P$^{@PTX}$ micelles, 19.48% of PTX was released in pH 7.4 PBS as the limited PTX and unoccupied diffuse channels from Fig. S5 (ESI†). Since PMAOEFC could be oxidized by 0.5% NaClO into poly(ferrocenium), PTX was release from P-DOX$^{@PTX\,dimer}$ along with the phase transformation of PMAOEFC. In view of a slow oxidize process of PMAOEFC, there was only 47.15% of PTX released in Fig. S6A(a) (ESI†). DOX was basically unaffected by the oxidation of NaClO, the release amount in Fig. S6(B) (ESI†) was almost consistent with Fig. 7B(f).

3.9 *In vitro* cytotoxicity

Cytotoxicity of nanovehicles is crucial for drug delivery. HeLa cells were treated using free PTX, DOX·HCl. Meanwhile, polymer P, P-DOX, P$^{@PTX}$, P-DOX$^{@PTX}$ and P-DOX$^{@PTX\,dimer}$ micellar solutions with different concentrations in MTT assay can reflect the cytotoxicity of all nanoformulations against L929 and HeLa cells. The significant cytotoxicity of free drugs was depicted in Fig. S7 (ESI†), 1.64 and 3.13 mg L^{-1} of IC_{50} was attributed to free DOX·HCl and PTX respectively, the higher IC_{50} of free PTX than that of DOX·HCl was related to poor blood circulation of hydrophobic PTX. L929 cells did not have abnormal physiological signals to induce drug release. Therefore, the cell viability was almost exceed 80% in Fig. 8(A). Especially, after treating with polymer P micelles for 48 h, cell viability of cells were higher than 88%, which was ascribed to the absence of drugs, showing the biocompatibility and potential of nanoformulations for drug delivery.[58] Less than 20% of cell apoptosis was caused by a small amount of drug release, consistent with *in vitro* drug release results at pH 7.4. On the contrary, the special physiological signals in HeLa cells lead to more drugs release from nanomicelles. As shown in Fig. 8(B), IC_{50} of P$^{@PTX}$, P-DOX, P-DOX$^{@PTX}$ and P-DOX$^{@PTX\,dimer}$, was 136.46, 49.32, 41.91 and 32.13 mg L^{-1}, equal to 1.64, 0.996 and 2.840 mg of PTX contained in P$^{@PTX}$, P-DOX$^{@PTX}$ and P-DOX$^{@PTX\,dimer}$ at IC_{50}, respectively. Similarly, 3.489, 3.395 and 2.272 mg of DOX was contained in P-DOX, P-DOX$^{@PTX}$ and P-DOX$^{@PTX\,dimer}$ in sequence. The sharp decrease of cell viability under the

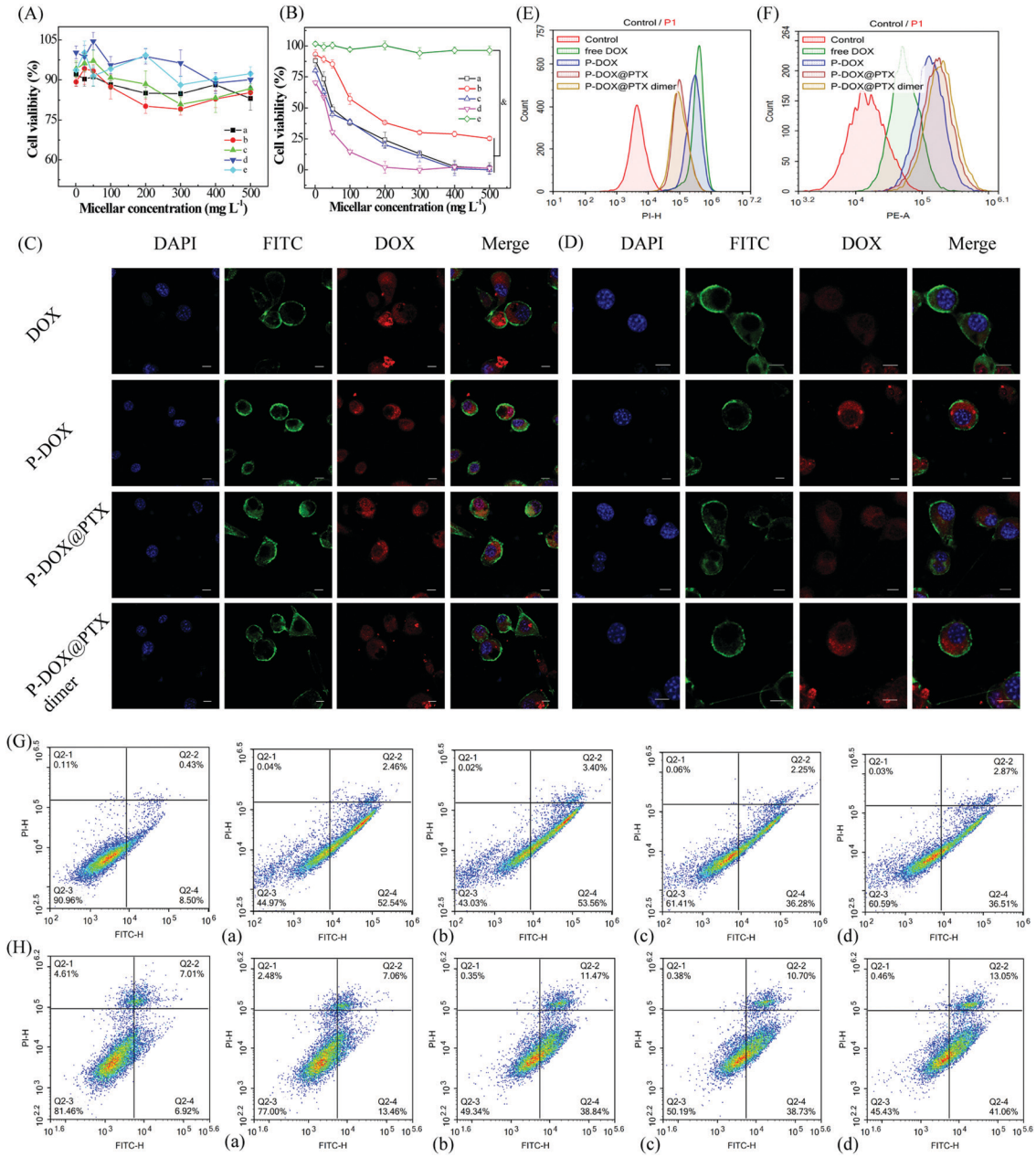

Fig. 8 The cytotoxicity of P-DOX (a), $P^{@PTX}$ (b), P-$DOX^{@PTX}$ (c), P-$DOX^{@PTX\,dimer}$ (d) and polymer P (e) micelles against L929 (A) and HeLa (B) cells, $^{\&}P < 0.001$. Qualitative analysis of cell uptake of DOX by CLSM in HCT116 (C) and HCT116/ADR (D) cells after 4 h incubation, scale bar =10 μm; quantitative analysis of cell uptake of DOX by FCM in HCT116 (E) and HCT116/ADR cells (F). Cell apoptosis of free DOX (a), P-DOX (b), P-$DOX^{@PTX}$ (c) and P-$DOX^{@PTX\,dimer}$ (d) in HCT116 (G) and HCT116/ADR cells (H).

treatment using nanoformulations signified the powerful lethality to HeLa cells, reflecting the great potential in cancer treatment.

3.10 Cellular uptake and apoptosis

To assess the intracellular drug internalization, accumulation, dispersion and content, HCT116 and HCT116/ADR cells were incubated with free DOX, P-DOX, P-$DOX^{@PTX}$ and P-$DOX^{@PTX\,dimer}$, then observed by confocal laser scanning microscope. Celluar uptake of DOX into HCT116 and HCT116/ADR cells after 1 h incubation was shown in Fig. S8 (ESI†). As displayed in Fig. 8(C), the red fluorescence was observed in cytoplasm and nucleus region, suggesting that the free DOX and nanoformulations could enter cells by diffusion and endocytosis, respectively. Compared with nanoformulation groups, the stronger intensity of nucleus of free DOX may be caused by direct diffusion into cell without being released from carrier. As for HCT119/ADR cells, the red fluorescence intensity of free DOX exhibited a slightly decrease than that of nanoformulations from Fig. 8(D), which is attributed to the

introduction of PTX. The combination of PTX and DOX could efficiently improve MDR effect through inhibiting P-gp efflux effect, resulting in enhanced internalization and accumulation in MDR cells. Free DOX across the cell membrane was through dispersion. A large number of DOX molecules were distributed around the cell nucleus, while the prepared nanocarriers can be uptaken mainly *via* endocytosis-lysosome approach.[62,63] Compared with cells treated with free DOX, the intensive red fluorescence emerged in P-DOX and P-DOX$^{@PTX\,dimer}$ groups, implying that the prepared nanoformulations could enahnce the cellular accumulation of the exogenous molecules. Moreover, P-DOX$^{@PTX\,dimer}$ presented higher permeability and retention efficiency than that of other groups, this was ascribed to the pH targeting effect of Schiff base and triple redox responsiveness of PMAOEFC, S–S bonds and Se–Se bonds,[64–66] where the fast delivery of DOX could be attributed to the acceleration during PTX release process. These results were also consistent with the higher DOX release content of P-DOX$^{@PTX\,dimer}$ in drug release study.

Furthermore, flow cytometry was utilized to quantitative analysis the above results, as presented in Fig. 8(E) and (F). There was almost no difference of internalized DOX for HCT116 cells after treatment using samples with or without PTX. However, the amount of internalized DOX increased according to the order of free DOX, P-DOX, P-DOX$^{@PTX}$ and P-DOX$^{@PTX\,dimer}$, which was in accordance with the above results from CLSM. These results demonstrated that the prepared PTX and DOX co-delivery system could inhibit P-gp efflux effect and improve drugs internalization and accumulation in MDR cells.

The apoptosis of HCT116 and HCT116/ADR cells were observed using flow cytometry after incubation with different samples for 4 h. As shown in Fig. 8(G), the apoptotic ratios of free DOX, P-DOX, P-DOX$^{@PTX}$ and P-DOX$^{@PTX\,dimer}$ were 55.00%, 56.96%, 38.53%, and 39.38% for HCT116 cells, respectively. The higher cell killing capacity of free DOX than nanoformulations is ascribed to different internalize pathway and time-lag drug release mode of carriers. By contrast, the slightly lower apoptotic

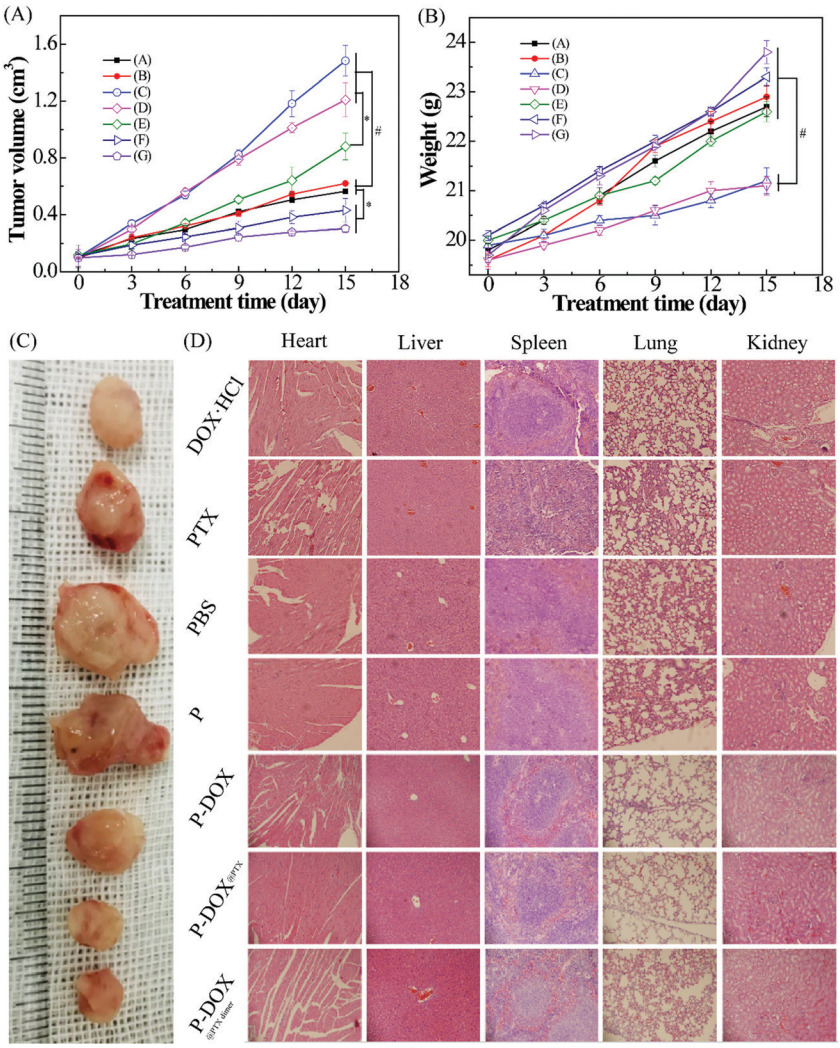

Fig. 9 Changes of tumor volume (A), body weight (B) of 4T1 bearing mice treated with DOX·HCl (a), PTX (b), PBS (c), P (d), P-DOX (e), P-DOX$^{@PTX}$ (f) and P-DOX$^{@PTX\,dimer}$ (g) at PTX and DOX dosage of 8 and 4 mg kg^{-1}, respectively. $^{\$}P < 0.001$, $^{\#}P < 0.01$ and $^{*}P < 0.05$. Photographs of excised tumor on day 15 after treatments (C) and histology H&E stain photograms of sliced major organs of mice on day 15 (200×) (D).

ratios of HCT116/ADR cells treated with free DOX and P-DOX from Fig. 8(H) were 20.52% and 50.31%, respectively. It is noteworthy that the significantly enhanced cytotoxicity of DOX occurs after PTX participation, leading to 49.43% of apoptotic ratio for P-DOX$^{@PTX}$ and 54.11% for P-DOX$^{@PTX\,dimer}$, respectively. These results suggest that PTX could improve DOX cytotoxicity bioavailability, meanwhile, the selenium containing DOX and PTX co-delivery system could overcome MDR effect efficiently by inhibiting P-gp overexpression.

3.11 *In vivo* antitumor efficacy

To assess the *in vivo* anticancer efficacy of a series of nanoformulas (P, P-DOX, P-DOX$^{@PTX}$, P-DOX$^{@PTX\,dimer}$), free drugs and PBS were injected into 4T1 bearing Balb/c mice every three days. The changes of tumor size and mice body weight from all groups are presented in Fig. 9. Although the tumor volumes of all groups were increased considerably after treatment with PBS, the ignorable tumor suppression effect was caused by the limited water solubility of free drugs.[9,60] For other groups, the tumors of P treated group had continuously growth because there was no anticancer drugs contained in P micelles, suggesting the good biocompatibility and bio-safety of the P micelles, as shown in Fig. 9A(d). Nanocarriers fabricated through chemical bonding and physical loading could promote drug content and improve stability of carriers, leading to a significant tumor inhibition. Especially, the P-DOX$^{@PTX\,dimer}$ micelles containing both DOX and PTX could enhance drug accumulation in solid tumor *via* EPR effect, as illustrated in Fig. 9A(g). This result may be ascribed to the prepared dual drugs co-delivery systems that could circumvent MDR effect. The apparent tumor suppression of P-DOX and P-DOX$^{@PTX}$ treated groups was observed in Fig. 9A(e and f), providing a promising treatment option for early stage tumors. The maximum TSR was approximately 79.57% for P-DOX$^{@PTX\,dimer}$ and 70.87% for P-DOX$^{@PTX}$ micelles, higher than that of 61.90% for free DOX·HCl and 58.13% for free PTX. Compared with the change trends of tumor size, body weight of mice treated with P-DOX$^{@PTX\,dimer}$ nanoformula increased miraculously, as displayed in Fig. 9B. It is noteworthy that the survival rate of all mice was 100% during treatment. Fig. 9C exhibited the isolated tumor photographs from all experimental groups, finding that the tumor size of groups treated with nanoformulas was reduced significantly and even almost all tumors are smaller than those treated with free drugs. In particular, P-DOX$^{@PTX\,dimer}$ presented a remarkable inhibition effect. These results were further attest the tumor size after 15 days treatment, which was in accordance with the results in Fig. 9A.

On the day of 15, all excised major organs were stained by H&E and observed to confirm the side effects during treatment, as listed in Fig. 9D. There was no markedly abnormalities of nanoformulas and PBS treated groups compared with the serious cardiotoxicity caused by free DOX·HCl and PTX.[67,68] In other words, the prepared nanovehicles could circumvent the side effects of free drugs, showing preeminent anticancer efficacy.[57]

4. Conclusion

In summary, the acid labile and multiple redox sensitive PEG-based PTX and DOX co-delivery systems were prepared through chemical bonding of DOX and physical loading of PTX (dimer). In particular, 39.3% of DOX and 49.1% of PTX were contained in P-DOX$^{@PTX\,dimer}$ nanovehicles, and EE of PTX had up to 97.0%. These nanocarriers can self-assemble into globular micelles with hydrophobic core comprising of PTX, DOX and PAMOEFC and hydrophilic shell including PEG and cystine. The destruction of micelles is attributable to the induction of cancerous physiological signals including pH 5.0, 10 mM GSH, 100 μM H_2O_2, *etc.*, causing drugs on-demand release. These nanoformulas not only circumvented the serious cardiotoxicity of free drugs, but also exhibited significant anticancer efficacy. To the potential for adjusting drugs content, improving stability and water solubility, overcoming MDR effect of tumors, these dual drugs co-delivery systems are expected to utilize in drug-resistant cancers sustainable treatment.

Conflicts of interest

There are no conflicts to declare.

Acknowledgements

We greatly acknowledge the financial support from the Fundamental Research Funds for the Central Universities (No. GK201601003), the National Natural Science Foundation of China (No. 21572123) and the Natural Science Research Fund of Shaanxi University of Science and Technology (No. 2019BJ-43).

References

1 D. D. Wisselink, L. L. F. Braakhuis, G. Gallo, W. M. U. van Grevenstein, S. van Dieren, N. F. M. Kok, P. R. de Reuver, P. J. Tanis and I. H. J. T. de Hingh, *Crit. Rev. Oncol. Hematol.*, 2019, **142**, 119–129.
2 D. Gu, K. Ladewig, M. Klimak, D. Haylock, K. M. McLean, A. J. O'Connor and G. G. Qiao, *Polym. Chem.*, 2015, **6**, 6475–6487.
3 Z. Z. Wu, Z. Y. Gan, B. Chen, F. Chen, J. Cao and X. L. Luo, *Biomater. Sci.*, 2019, **7**, 3190–3203.
4 A. K. Swain, L. Pradhan and D. Bahadur, *ACS Appl. Mater. Interfaces*, 2015, **7**, 8013–8022.
5 K. A. Kosakowska, B. K. Casey, S. L. Kurtz, L. B. Lawson and S. M. Grayson, *Biomacromolecules*, 2018, **19**, 3163–3176.
6 M. C. Koester, W. R. Dunn, J. E. Kuhn and K. P. Spindler, *J. Am. Acad. Orthop. Surg.*, 2007, **15**, 3–11.
7 M. Q. Gong, C. Wu, X. Y. He, J. Y. Zong, J. L. Wu, R. X. Zhuo and S. X. Cheng, *Pharm. Res.*, 2017, **34**, 148–160.
8 Q. Yin, J. N. Shen, Z. W. Zhang, H. J. Yu and Y. P. Li, *Adv. Drug Delivery Rev.*, 2013, **65**, 1699–1715.
9 Q. H. Feng, Y. Y. Zhang, W. X. Zhang, X. N. Shan, Y. J. Yuan, H. L. Zhang, L. Hou and Z. Z. Zhang, *Acta Biomater.*, 2016, **38**, 129–142.

10 D. Li, Y. T. Zhang, S. Jin, J. Guo, H. F. Gao and C. C. Wang, *J. Mater. Chem. B*, 2014, **2**, 5187–5194.
11 Q. Xu, W. J. Huang, L. B. Jiang, Z. J. Lei, X. Y. Li and H. B. Deng, *Carbohydr. Polym.*, 2013, **97**, 565–570.
12 M. K. Cho, A. Gayen, J. R. Banigan, M. Leninger and N. J. Traaseth, *J. Am. Chem. Soc.*, 2014, **136**, 8072–8080.
13 N. Joubert, C. Denevault-Sabourin, F. Bryden and M. C. Viaud-Massuard, *Eur. J. Med. Chem.*, 2017, **142**, 393–415.
14 F. Xu, H. Li, Y. L. Luo and W. Tang, *ACS Appl. Mater. Interfaces*, 2017, **9**, 5181–5192.
15 G. R. Qiu, X. Liu, B. R. Wang, H. B. Gu and W. X. Wang, *Polym. Chem.*, 2019, **10**, 2527–2539.
16 A. Raza, U. Hayat, T. Rasheed, M. Bilal and H. M. N. Iqbal, *Eur. J. Med. Chem.*, 2018, **157**, 705–715.
17 W. J. Yang, T. T. Zhao, P. Zhou, S. M. Chen, Y. Gao, L. J. Liang, X. D. Wang and L. H. Wang, *Polym. Chem.*, 2017, **8**, 3056–3065.
18 J. L. Zhang, R. S. Srivastava and R. D. K. Misra, *Langmuir*, 2007, **23**, 6342–6351.
19 Y. X. Zhang, R. J. Yin, G. Z. Wu, M. M. Yu, J. N. Liu, X. T. Wang, X. M. Liu, H. S. Guan, R. L. Yu and T. Jiang, *Eur. J. Med. Chem.*, 2020, 200.
20 A. G. Cheetham, R. W. Chakroun, W. Ma and H. G. Cui, *Chem. Soc. Rev.*, 2017, **46**, 6638–6663.
21 Y. J. Wang, D. Liu, Q. C. Zheng, Q. Zhao, H. J. Zhang, Y. Ma, J. K. Fallon, Q. Fu, M. T. Haynes, G. M. Lin, R. Zhang, D. Wang, X. G. Yang, L. X. Zhao, Z. G. He and F. Liu, *Nano Lett.*, 2014, **14**, 5577–5583.
22 H. X. Wang, H. Y. Xie, J. G. Wang, J. P. Wu, X. J. Ma, L. L. Li, X. Y. Wei, Q. Ling, P. H. Song, L. Zhou, X. Xu and S. S. Zheng, *Adv. Funct. Mater.*, 2015, **25**, 4956–4965.
23 H. Jin, M. Sun, L. L. Shi, X. Y. Zhu, W. Huang and D. Y. Yan, *Biomater. Sci.*, 2018, **6**, 1403–1413.
24 J. W. Xu, X. Ge, L. H. Lv, F. Xu and Y. L. Luo, *Macromol. Rapid Commun.*, 2018, 39.
25 D. Vinciguerra, M. Jacobs, S. Denis, J. Mougin, Y. Guillaneuf, G. Lazzari, C. Zhu, S. Mura, P. Couvreur and J. Nicolas, *J. Controlled Release*, 2019, **295**, 223–236.
26 F. Q. Guo, Z. X. Fan, J. B. Yang, Y. Li, Y. G. Wang, H. Zhao, L. Y. Xie and Z. Q. Hou, *Nanoscale Res. Lett.*, 2016, 11.
27 C. Roberge, J. M. Cros, J. Serindoux, M. E. Cagnon, R. Samuel, T. Vrlinic, P. Berto, A. Rech, J. Richard and A. Lopez-Noriega, *J. Controlled Release*, 2020, **319**, 416–427.
28 P. Saint-Cricq, S. Deshayes, J. I. Zink and A. M. Kasko, *Nanoscale*, 2015, **7**, 13168–13172.
29 L. Sun, H. Wei, X. S. Zhang, C. Meng, G. Y. Kang, W. Ma, L. W. Ma, B. Y. Wang and C. Y. Yu, *Polym. Chem.*, 2020, **11**, 4469–4476.
30 H. Y. Wen, H. Q. Dong, W. J. Xie, Y. Y. Li, K. Wang, G. M. Pauletti and D. L. Shi, *Chem. Commun.*, 2011, **47**, 3550–3552.
31 G. Y. Zhang, X. L. Li, Q. B. Liao, Y. F. Liu, K. Xi, W. Y. Huang and X. D. Jia, *Nat. Commun.*, 2018, 9.
32 A. Hernandez-Montoto, M. Gorbe, A. Llopis-Lorente, J. M. Terres, R. Montes, R. Cao-Milan, B. D. de Grenu, M. Alfonso, M. Orzaez, M. D. Marcos, R. Martinez-Manez and F. Sancenon, *Chem. Commun.*, 2019, **55**, 9039–9042.
33 C. A. Metcalf, S. Svenson, J. Hwang, S. Tripathi, G. Gangal, S. Kabir, D. Lazarus, R. Cole, B. Sweryda-Krawiec, P. Shum, D. Brown, R. I. Case, D. van der Poll, E. Rohde, S. Harlfinger, C. H. Teng and S. Eliasof, *J. Med. Chem.*, 2019, **62**, 9541–9559.
34 R. Reid, M. Sgobba, B. Raveh, G. Rastelli, A. Sali and D. V. Santi, *Macromolecules*, 2015, **48**, 7359–7369.
35 H. Y. Wen, C. Y. Dong, H. Q. Dong, A. J. Shen, W. J. Xia, X. J. Cai, Y. Y. Song, X. Q. Li, Y. Y. Li and D. L. Shi, *Small*, 2012, **8**, 760–769.
36 M. Z. Xu, C. Y. Zhang, J. G. Wu, H. G. Zhou, R. Bai, Z. Y. Shen, F. L. Deng, Y. Liu and J. Liu, *ACS Appl. Mater. Interfaces*, 2019, **11**, 5701–5713.
37 E. Dominguez-Alvarez, M. Gajdacs, G. Spengler, J. A. Palop, M. A. Marc, K. Kiec-Kononowicz, L. Amaral, J. Molnar, C. Jacob, J. Handzlik and C. Sanmartin, *Bioorg. Med. Chem. Lett.*, 2016, **26**, 2821–2824.
38 G. Spengler, M. Evaristo, J. Handzlik, J. Serly, J. Molnar, M. Viveiros, K. Kiec-Kononowicz and L. Amaral, *Anticancer Res.*, 2010, **30**, 4867–4871.
39 Y. Zhou, H. Y. Wen, L. Gu, J. J. Fu, J. Y. Guo, L. R. Du, X. Q. Zhou, X. Y. Yu, Y. G. Huang and H. Wang, *J. Nanobiotechnol.*, 2017, 15.
40 H. C. Kim, E. Kim, T. L. Ha, S. W. Jeong, S. G. Lee, S. J. Lee and B. Lee, *Colloids Surf., B*, 2015, **127**, 206–212.
41 X. W. Guan, Y. H. Li, Z. X. Jiao, J. Chen, Z. P. Guo, H. Y. Tian and X. S. Chen, *Acta Biomater.*, 2013, **9**, 7672–7678.
42 D. J. Zhao, J. L. Wu, C. X. Li, H. Y. Zhang, Z. H. Li and Y. X. Luan, *Colloids Surf., B*, 2017, **155**, 51–60.
43 N. N. Li, L. X. Zhao, L. S. Qi, Z. H. Li and Y. X. Luan, *Prog. Polym. Sci.*, 2016, **58**, 1–26.
44 J. J. Sun, Y. H. Liu, Y. C. Chen, W. C. Zhao, Q. Y. Zhai, S. Rathod, Y. X. Huang, S. Q. Tang, Y. T. Kwon, C. Fernandez, R. Venkataramanan and S. Li, *J. Controlled Release*, 2017, **258**, 43–55.
45 K. E. Washington, R. N. Kularatne, M. C. Biewer and M. C. Stefan, *ACS Biomater. Sci. Eng.*, 2018, **4**, 997–1004.
46 S. Honda, T. Yamamoto and Y. Tezuka, *Nat. Commun.*, 2013, 4.
47 S. C. Owen, D. P. Y. Chan and M. S. Shoichet, *Nano Today*, 2012, **7**, 53–65.
48 J. Logie, S. C. Owen, C. K. McLaughlin and M. S. Shoichet, *Chem. Mater.*, 2014, **26**, 2847–2855.
49 Y. Wang, Y. L. Luo, F. Xu, Y. S. Chen and W. Tang, *J. Ind. Eng. Chem.*, 2017, **48**, 66–78.
50 Y. Q. Xu, L. Wang, Y. K. Li and C. Q. Wang, *Carbohydr. Polym.*, 2014, **114**, 27–35.
51 J. Kim, H. Kim and W. J. Kim, *Small*, 2016, **12**, 1184–1192.
52 M. L. Tintas, L. Foucout, S. Petit, S. Oudeyer, F. Gourand, L. Barre, C. Papamicael and V. Levacher, *Eur. J. Med. Chem.*, 2014, **81**, 218–226.
53 C. Y. Ang, S. Y. Tan, C. Teh, J. M. Lee, M. F. E. Wong, Q. Y. Qu, L. Q. Poh, M. H. Li, Y. Y. Zhang, V. Korzh and Y. L. Zhao, *Small*, 2017, 13.
54 G. Ghimire, Y. Yi, M. A. Derylo, L. A. Baker and T. Ito, *Langmuir*, 2015, **31**, 12307–12314.

55 X. W. Peng, P. W. Liu, B. Pang, Y. W. Yao, J. X. Wang and K. Zhang, *Carbohydr. Polym.*, 2019, **216**, 113–118.
56 L. L. Wang, B. C. Tian, J. Zhang, K. K. Li, Y. Liang, Y. J. Sun, Y. Y. Ding and J. T. Han, *Int. J. Pharm.*, 2016, **501**, 221–235.
57 K. Dong, Z. Liu, Z. H. Li, J. S. Ren and X. G. Qu, *Adv. Mater.*, 2013, **25**, 4452–4458.
58 J. J. Li, W. D. Ke, H. Li, Z. S. Zha, Y. Han and Z. S. Ge, *Adv. Healthcare Mater.*, 2015, **4**, 2206–2219.
59 C. Chen, J. L. Zhou, X. Han, F. Song, X. L. Wang and Y. Z. Wang, *Nanotechnology*, 2014, 25.
60 J. Z. Du, X. J. Du, C. Q. Mao and J. Wang, *J. Am. Chem. Soc.*, 2011, **133**, 17560–17563.
61 L. C. Liu, L. L. Rui, Y. Gao and W. A. Zhang, *Polym. Chem.*, 2015, **6**, 1817–1829.
62 Y. H. Duo, Y. Li, C. K. Chen, B. Y. Liu, X. Y. Wang, X. W. Zeng and H. B. Chen, *RSC Adv.*, 2017, **7**, 39641–39650.
63 C. G. Liu, Y. H. Han, J. T. Zhang, R. K. Kankala, S. B. Wang and A. Z. Chen, *Chem. Eng. J.*, 2019, **370**, 1188–1199.
64 B. Yu, S. Goel, D. L. Ni, P. A. Ellison, C. M. Siamof, D. W. Jiang, L. Cheng, L. Kang, F. Q. Yu, Z. Liu, T. E. Barnhart, Q. J. He, H. Zhang and W. B. Cai, *Adv. Mater.*, 2018, 30.
65 H. Xing, K. Hwang and Y. Lu, *Theranostics*, 2016, **6**, 1336–1352.
66 A. E. Hansen, A. L. Petersen, J. R. Henriksen, B. Boerresen, P. Rasmussen, D. R. Elema, P. M. af Rosenschold, A. T. Kristensen, A. Kjaer and T. L. Andresen, *ACS Nano*, 2015, **9**, 6985–6995.
67 Z. Jin, K. Q. Wu, J. W. Hou, K. H. Yu, Y. Y. Shen and S. R. Guo, *Biomaterials*, 2018, **153**, 49–58.
68 R. R. Zhu, Z. Q. Wang, P. Liang, X. L. He, X. Z. Zhuang, R. Q. Huang, M. Wang, Q. G. Wang, Y. C. Qian and S. L. Wang, *Acta Biomater.*, 2017, **63**, 163–180.

